Doctoral Dissertation

Neural Bases for Discriminating the Temporal Direction of Time's Arrow: An Awake Monkey fMRI Study

Reiji Tanaka

March 2025

Abstract

Time flows in one direction, a physical constraint humans recognize, as reflected in proverbs such as “there is no crying over spilt milk”. Recent studies from our laboratory have shown that human participants rely on specific cues to discriminate the direction of time's arrow, and functional magnetic resonance imaging (fMRI) has suggested the existence of neural networks that show selectivity for temporal directionality. These neural bases are likely shared across species, as the physical constraint is universal, even if other species may not “recognize” it as a law. This dissertation aims to elucidate these neural bases through whole-brain fMRI in awake monkeys, investigating whether and how the non-human primate brain discriminates the direction of time’s arrow.

A significant methodological contribution of this paper is the development of a completely non-invasive head restraint method using thermoplastic masks, described in Chapter 2. This method facilitates high-quality fMRI data acquisition while minimizing the effort and cost of experiment preparation, as well as the burden on the monkeys, addressing longstanding challenges in awake monkey fMRI research. The method not only enhances data reliability but also aligns with ethical principles in animal research.

In the main experimental study (Chapter 3), monkeys were presented with video clips depicting biological and non-biological motion under three conditions: normal (forward and upright), temporally reversed, and spatially inverted. Whole-brain analyses revealed that the superior temporal sulcus (STS) and related cortical regions preferentially responded to temporally forward and spatially upright biological motion, reflecting sensitivity to naturalistic dynamics in both temporal and spatial domains. Additionally, subcortical structures, including the superior colliculus and pulvinar, were implicated in detecting temporal coherence in biological motion, suggesting their role in a subcortical-cortical network for discriminating the direction of time’s arrow. Conversely, reverse playback of non-biological motion elicited robust activation in the cerebellum and the STS, suggesting involvement in prediction-error processing triggered by unexpected or nonsensical motion.

These findings advance our understanding of the neural substrates of time perception by highlighting the distinct contributions of cortical and subcortical regions in discriminating the direction of time’s arrow. The methodological advancements and experimental insights presented in this dissertation lay the groundwork for future research into the neural circuits underlying time perception in primates, with implications for understanding the evolution of temporal cognition and its neural basis.

Table of Contents

Abstract 2
Table of Contents 3
Chapter 1 General Introduction 5
1.1. General Background 5
1.2. Purpose of the Dissertation 5
1.3. Structure of the Dissertation 6
1.4. References 6
Chapter 2 An easy-to-implement, non-invasive head restraint method for monkey fMRI 7
2.1. Introduction 7
2.2. Methods and Materials 8
2.2.1. Subjects 8
2.2.2. Plastic mask details 8
2.2.3. Optimal shape of the mask 9
2.2.4. Details of head-post implants used for comparison with the plastic mask 10
2.2.5. Training 10
2.2.6. MR data acquisition 11
2.2.7. Visual Stimuli 11
2.2.8. FMRI data preprocessing 12
2.2.9. Functional image analysis 12
2.2.10. Movement estimation 12
2.3. Results 13
2.3.1. Progress of pre-scan training 13
2.3.2. Examination of fMRI data quality 13
2.3.3. Examination of head movements 14
2.3.4. Retinotopic mapping 16
2.3.5. Upper limit of scan duration using masks 17
2.4. Discussion 18
2.5. Figures 21
2.6. References 28
Chapter 3 Neural Bases for Discriminating the Temporal Direction of Time's Arrow: An Awake Monkey fMRI Study 30
3.1. Introduction 30
3.2. Methods and Materials 31
3.2.1. Subjects 31
3.2.2. Visual stimuli 32
3.2.3. MR data acquisition 33
3.2.4. FMRI data preprocessing 33
3.2.5. Functional image analysis 34
3.3. Results 35
3.3.1. Validation of the non-invasive head-restraint technique 35
3.3.2. Experiment 1 (Forward/Reverse) 35

3.3.3. Experiment 2 (Upright/Inverted)....37
Cortical regions specific for temporal and spatial processing....38
3.4. Discussion....38
3.4.1. The SC and the STS preferentially detect biological motions that are more physically plausible....39
3.4.2. Why the GLM analysis failed to fully capture the forward-preferential response in the SC....39
3.4.3. Role of the STS and cerebellum in prediction-error coding during naturalistic motion perception....40
3.4.4. Preference of the arcuate sulcus for upright-played videos....40
3.4.5. Conclusion....41
3.5. Figures and Tables....42
3.6. References....60
Chapter 4 General Discussion....62
Advancements in Methodology of Awake Monkey fMRI....62
Neural Bases for Discriminating Time's Arrow....62
Differences Between Monkey and Human fMRI Findings....63
Acquisition of the Concept of "Time's Arrow"....63
Implications and Future Directions....64
References....65
Chapter 5 Achievements....66
5.1. Papers....66
5.2. Presentations....66

Chapter 1
General Introduction

1.1. General Background

The perception of time, the ability to discern the flow and direction of events, is a cornerstone of cognition that allows organisms to adapt to and interact with a dynamic world. We believe that time flows from the past into the present and proceeds toward the future. This phenomenon is referred to as "time's arrow" (Eddington, 1928). This perception is deeply rooted in our ability to predict future states, interpret environmental cues, and coordinate motor actions. Behavioral studies have demonstrated that humans can reliably judge temporal order and directionality, even for events separated by only a few milliseconds (Hirsh & Sherrick, 1961; Pöppel, 1997). However, this capacity is highly context-dependent and malleable, influenced by prior experience, attention, and sensory plausibility.

Recent advances in neuroscience have begun to unravel the neural mechanisms underlying time perception. Human fMRI studies have implicated cortical regions, such as the temporo-occipital junction and middle temporal gyrus, as well as subcortical structures, including the cerebellum, in the processing of temporal coherence (Hanyu et al., 2023b, conference presentation; Maffei et al., 2015). Additionally, neural recording studies in monkeys reported that neurons in the anterior superior temporal sulcus exhibited stronger responses to forward than to backward walking motion. These findings suggest that time-flow perception emerges from a complex interaction between cortical and subcortical networks. Despite these insights, our understanding remains incomplete, particularly in non-human primates, whose neural circuits share remarkable similarities with humans but remain underexplored in this context.

Functional magnetic resonance imaging (fMRI) in awake monkeys provides a powerful tool to bridge this gap, enabling detailed investigations into the neural circuits underlying the ability to discriminate the temporal direction of time's arrow. However, the inherent challenges of awake monkey fMRI, such as head motion and animal stress, have limited its application. Addressing these challenges is essential for advancing our understanding of the fundamental neural mechanisms of time perception and their evolutionary origins.

1.2. Purpose of the Dissertation

The primary aim of this dissertation is to investigate the neural bases for discriminating the temporal direction of time's arrow in non-human primates. Specifically, this work seeks to:

1. Develop a non-invasive head restraint method for awake monkey fMRI.
2. Determine whether monkeys possess specialized neural circuits for processing the temporal direction of visual stimuli.

To achieve these goals, this dissertation is divided into two major components. The first (Chapter 2) involves the development of a novel, non-invasive head restraint method using thermoplastic masks, designed to overcome technical limitations in awake monkey fMRI. The second component (Chapter 3) applies this method to investigate the neural substrates underlying the perception of time's arrow by comparing brain activations in monkeys during the presentation of natural video stimuli in forward- and reverse-playback.

1.3. Structure of the Dissertation

This dissertation comprises following five chapters:

- Chapter 1: provides an overview of the dissertation, including the general background, research purpose, and structural organization.
- Chapter 2: introduces a completely non-invasive head restraint system for awake monkey fMRI. This chapter details the development, implementation, and evaluation of this method, emphasizing its advantages over conventional invasive techniques.
- Chapter 3: presents the main experimental study investigating the neural bases of the perception of time's arrow in awake monkeys. Videos of biological and non-biological motion were presented in forward and temporally-reversed playback conditions to examine how temporal coherence of motions influence neural activity.
- Chapter 4: discusses the broader implications of the findings, integrating insights from both the methodological and experimental studies. This chapter also highlights the limitations of the current work and outlines potential directions for future research.
- Chapter 5: lists my academic achievements, including published papers and conference presentations, which are directly related to the research presented in this dissertation.

1.4. References

Eddington, S. A. S. (1928). The Nature of the Physical World. New York, The Macmillan Company; Cambridge, Eng., The University Press.

Hanyu, N., Watanabe, K., & Kitazawa, S. (2023a). Ready to detect a reversal of time's arrow: a psychophysical study using short video clips in daily scenes. Royal Society Open Science, 10(4).

Hanyu, N., Watanabe, K., & Kitazawa, S. (2023b, October 4). Neural bases for judging the direction of time's arrow. Proceedings Timing Research Forum 3.

Hirsh, I. J., & Sherrick, C. E. , Jr. (1961). Perceived order in different sense modalities. Journal of Experimental Psychology, 62(5), 423–432.

Maffei, V., Giusti, M. A., Macaluso, E., Lacquaniti, F., & Viviani, P. (2015). Unfamiliar Walking Movements Are Detected Early in the Visual Stream: An fMRI Study. Cerebral Cortex, 25(8), 2022–2034.

Pöppel, E. (1997). A hierarchical model of temporal perception. Trends in Cognitive Sciences, 1(2), 56–61.

Chapter 2
An easy-to-implement, non-invasive head restraint method for monkey fMRI

2.1. Introduction

Functional magnetic resonance imaging (fMRI) in behaving monkeys has become increasingly popular in cognitive neuroscience (Vanduffel, et al., 2001; Ku et al., 2011). It has a potential to bridge the gap between human fMRI and monkey electrophysiology studies. However, there are still several problems that need to be solved in monkey fMRI, which could discourage those interested in this field from participating in it. These problems include motion artifacts caused by head and body movements, magnetic field susceptibility caused by head-restraint implants, and signal dropout caused by an air-filled gap along the body margin (e.g., back of the neck). To overcome these problems, researchers have long strived to develop effective protocols; these include optimization of the seating posture (Logothetis et al., 1999; Miyamoto, et al., 2017), use of a contrast-enhancing agent (Vanduffel, et al., 2001), optimization of coil position, the direction of phase-encoding, and the implant type and location (Srihasam et al., 2010; Oritz-Rios, et al., 2018).

The present report describes a novel method for head restraint of awake monkeys in an MRI scanner using only a plastic head mask. This mask is easy to make and does not require any invasive procedures. In behavioral neurophysiology, a previous report has described the effectiveness of plastic masks for head-restraint in neuronal recording in awake monkeys (Drucker et al., 2015). By refining this method, I have found that a plastic mask can be used in fMRI experiments, which require tighter head restraint than neurophysiological experiments. The present plastic head mask is made of a standard thermoplastic splint material that is softened by hot water so that it can be deformed. It was molded so that it conformed to the contours of the animal's scalp (skull), zygomatic bones and occipital ridge. No surgical implant was required from the early acclimatization process to the behavioral scan sessions.

The present technique has several advantages over the conventional invasive head-post method. First, since no surgical procedures are required, there is no risk of infection or pain from surgical wounds, thus greatly reducing the stress on animals. This not only conforms to the spirit of the 3R's, but could also mean that a lower level of pain could be declared in the ethical review for animal experiments. Second, because the monkey's head, from the surface of the brain to the scalp, is kept completely intact, the BOLD signal is free of artifact-related (implant-derived) noise. Third, because the material needed to create one head mask (i.e., one piece of commercially available splint material) costs only about 50 US dollars and because it requires only a single brief general anesthesia session (about 30–40 minutes) to make one head mask, the cost and time required for this method are less than those in the conventional methods that require surgery.

Using the plastic mask, I trained three monkeys in a fixation task for retinotopic mapping. All of them rarely showed abrupt head movements that appeared as spikes in an x, y or z translation plot in the post-hoc image realignment. I was able to obtain reliable retinotopic BOLD responses in the standard visual meridian localizers. The present study demonstrates that the use of a non-invasive plastic mask works well in fMRI experiments in awake monkeys. I describe points to consider in creating a mask that effectively suppresses head movement.

2.2. Methods and Materials

2.2.1. Subjects

I used three female Japanese monkeys (Macaca fuscata, monkeys B, R and T): 7, 5 and 5 years old weighing 6, 7 and 6 kg, respectively. None of the monkeys had any head-post implants before or during this study. Monkey B had 9 months of daily training in a mock scanner prior to the scan. During this 9-month period, monkey B was used to optimize the present plastic mask method. Monkeys R and T were trained daily for 3 months before the scan. For these two monkeys, training was carried out according to a pre-planned training regimen which I developed based on prior experience with monkey B. The experimental procedures were approved by the Animal Research Committee at the Graduate School of Frontier Biosciences, Osaka University, and were in full compliance with the guidelines of the National BioResource Project "Japanese Macaques" and the National Institutes of Health guide for the care and use of Laboratory animals.

2.2.2. Plastic mask details

The plastic mask for head immobilization was made using a medical plastic splint material (Figure 2.1A) (product number: MTAPUR, 3.2-mm thick, CIVCO Radiotherapy, Orange City, IA) which is usually used to inhibit body movements of human patients during radiotherapy treatment. For monkey T, as I discuss later, part-way through the fMRI data collection, I remade the mask using more solid material (product number: MTAPUIR2232, 3.2-mm thick, CIVCO Radiotherapy, Iowa). To make plastic masks, I first anaesthetized a monkey with medetomidine (0.1 mg/kg, i.m.) and ketamine (2.5 mg/kg, i.m.) and placed it on a horizontal MRI chair (Figure 2.1B). I manually fixed the monkey's head at the desired height and axial location (Figure 2.1B). Since, in an anaesthetized monkey, the head position tends to sink lower than the usual position at which the monkey faces a screen and sucks a drinking spout during the experiment, I recommend pre-fixing a drinking spout to the chair at the height normally used by monkeys, and to manually hold the monkey's head at that position until the entire production process is completed (Figure 2.1B).

While one person held the head of the monkey, another soaked one piece of the U-shaped splint material in boiling water (> 90°C) until it was softened (1–2 minutes) (Figure 2.1C). Before the softened splint material was applied to the monkey, it was quickly dried with paper towels and cooled to under 50°C. The softened material was placed directly on the monkey's head with the straight end of the U-shaped material placed at the level of the monkey's nose, and molded by hand to fit the contours of the

monkey's scalp (skull), zygomatic bones and occipital ridge (Figure 2.1D). Even after the initial shape of the plastic mask was determined, I held the splint material and the monkey's head firmly in place for a few minutes until the splint material cooled and hardened. After the material regained its stiffness, I used a permanent marker pen to draw cut-here lines on the area of the mask covering the eyes and ears. I also marked the locations at the base of the mask where the M6 screws would penetrate to contact screw holes on the monkey chair (Figure 2.1E). I fixed the mask to the chair with four M6 screws (top, bottom, left and right of the protruding part of the monkey head of the mask). During a single anesthesia session in one monkey (about 30–40 min), I would usually make two to three masks, and I selected the best one among them. After returning the monkey to the cage, I verified that the selected mask could be fitted to the chair with four M6 screws (Figure 2.1F).

I selected the mask based on the following criteria: 1) the mask did not interfere with head coils; 2) the monkey did not show any signs of discomfort when wearing the mask; 3) the mask did not bend when the monkey moved its lower body; and 4) movement of the head when drinking from spout was minimal (i.e., slight jaw movements during drinking did not propagate to the top of the head. This is usually achieved by not completely covering the lower jaw with the mask).

On the following day, I put the monkey on the chair without anesthesia and checked the fitting of the mask (Figure 2.1G). If there were places that were too tight or loose, I took the mask off the monkey and used a soldering iron to partially soften and deform the mask. I then put the mask back on the monkey and checked the fit. Once it was confirmed that the mask fit the monkey's head tightly, task training began from the next session. I did not shave or trim the monkey's fur. No side effects such as swelling or bruising were observed after more than one year of use.

2.2.3. Optimal shape of the mask

To minimize head movement during experiments, it is critical to fit the mask to the shape of the monkey's head as tight as possible. Through trial-and-error, I found two critical locations on the skull: the zygomatic bones and the occipital ridge (Figure 2.1H, cyan and red arrows, respectively). Pressing the softened thermoplastic tightly against the contours of the zygomatic bones and the occipital ridge is crucial for achieving an optimal fit of the mask. Figure 2.1H shows an example of how these two locations are molded as closely as possible relative to the monkey’s head. In this mask, the plastic is firmly pressed just below the zygomatic bones (cyan arrows). This tight fit prevents the zygomatic bones from being displaced upward and downward from their original position in the mask. The plastic tightly adheres to the occipital ridge, leaving a gap between the occipital area and the neckplate of the chair (red arrows). This portion of the splint on the occipital ridge held the head down from above.

Fitting the mask optimally around the monkey’s head not only reduces head movement, but also allows the head coil to be positioned as close as possible to the monkey's head. Figure 2.1I shows the two different types of coils I used. I was able to bring both coils close enough to the monkey's head to acquire EPI images of the whole brain. Use of the optimally shaped mask allows placement of a multichannel coil as close to the head as possible (Figure 2.1I, bottom).

2.2.4. Details of head-post implants used for comparison with the plastic mask

To assess the quality of fMRI images obtained with the plastic mask, I compared the images with those obtained in another monkey whose head was restrained by a standard PEEK head-post. The fMRI images of this monkey were obtained in a different experiment prior to the present study in my laboratory.

The head post was designed at the National Institute for Physiological Sciences (Okazaki, Japan) and manufactured by a workshop in Osaka University. The head post had a trapezoidal cross-section (top 15 mm, bottom 20 mm, height 15 mm) and a height of 35 mm. This trapezoidal column was connected at its bottom to a disk-shaped base 26 mm in diameter and 10 mm high. This disk-shaped base was placed directly on the skull with its center located at stereotaxic coordinates of AP 15.5 mm and ML 0 mm. The bone screws were commercially-available pan head screws (M3L5) made of PEEK (part number PE-0305, Wilco Inc. Yokohama, Japan). I implanted 18 of these from the occipital to the temporal region of the skull as anchors for dental cement.

2.2.5. Training

Behavioral training was conducted 5 days per week outside the scanner. Access to water was restricted in the monkeys' home cages except for weekends. The monkeys sat in a custom-made horizontal primate chair in a "sphinx" position in a mock MR bore placed in a dimly lit, sound-attenuated cubicle. Visual stimuli were presented on a standard 19-in. TFT monitor (DELL) placed 56 cm from the monkey's face. Eye movements were monitored at 120 Hz using an infrared eye tracking system (EyeLink 1000, SR Research). MATLAB Psychtoolbox was used to present stimuli, control the task events and acquire behavioral data.

Training was conducted in a step-by-step manner (Figure 2.2A,B). After the monkeys were acclimated to head-restraint by the plastic mask and trained to drink from a spout (termed "acclimatization to head-restraint" and "spout-training"), calibration for eye movement tracking was conducted ("calibration"). Subsequently, the monkeys were trained in a standard fixation task ("fixation task (trial-by-trial)") and in a continuous version of the fixation task in which fixation point (FP) was presented continuously for 2–4 minutes. To encourage continuous fixation within a square fixation window (6.1° on a side), rewards (drop of fruit juice) were given while their gaze was in the window, and the inter-reward interval was shortened step-wise from 2,500-ms to 500-ms as fixation continued without a fixation break (FB). When the monkey made a FB, the inter-reward interval was reset to the initial value (2,500-ms). After fixation performance reached an asymptote (about 90%), visual stimuli were presented for the standard visual meridian and eccentricity localizer scans (wedge and annulus stimuli) were added to the fixation task (see below).

I used a relatively large fixation window compared to those which are often used in vision neuroimaging studies (e.g., 2.0° on a side), but not because there was a problem with measuring eye movement or a problem with head stability when I used the plastic mask. Instead, this was because the ultimate goals of my monkey fMRI experiments were to study brain activity in cognitive tasks (which usually involve a fixation window larger than those used in visual experiments) and brain activity during free viewing of various visual stimuli. For these purposes, it was not necessary for us to make the fixation

window smaller than necessary. In addition, I confirmed that although I used a relatively large fixation window (6.1° × 6.1°), the monkeys' gaze location during the fixation task was located predominantly within a smaller, imaginary 2.0° × 2.0° fixation window (see Figure 2.6B and the corresponding section in the Results).

2.2.6. MR data acquisition

The blood oxygen level-dependent (BOLD) signal was measured by the echo planner imaging (EPI) method using a 3T Magnetom Prisma-Fit MRI scanner (Siemens, München, Germany). A custom-made phased-array 12-ch receiver coil (Takashima Seisakusho Co., Ltd., Tokyo, Japan) was fitted around the mask, covering the entire brain of the monkey. Each daily session consisted of three or four functional scans which I called "runs". Each run lasted 272 seconds, using the following parameters: repetition time (TR) = 2 s; echo time (TE) = 30 ms; flip angle = 75°; 86 × 86 matrix; voxel size = 1.5 mm isotopic; 62 slices; and phase encoding direction (PE) = anterior/posterior (A/P). For the image distortion correction (topup processing), five EPI images of PE = P/A were also obtained in each session. The first eight volumes of each run were discarded to cut off initial steady-state problems.

In a separate session, higher resolution T1-weighted anatomical images were obtained with monkeys anaesthetized by medetomidine (0.03 mg/kg, i.m.), midazolam (0.2 mg/kg, i.m.) and butorphanol tartrate (0.3 mg/kg, i.m.). I used a 1-channel loop coil (Takashima Seisakusho Co., Ltd.) and the following parameters: TR = 1.5 s; TE = 1.92 ms; flip angle = 8°; 192 × 192 matrix; voxel size = 0.67 mm isotopic; and 192 slices. Six, three and four structural scans were taken for monkeys B, R and T, respectively, and averaged for each monkey.

2.2.7. Visual Stimuli

Inside the MRI scanner, visual stimuli were backprojected to a screen placed 56 cm from the monkey's eyes. The size of the projection was 34.9° × 28.3° of visual angle (1280 × 1024 pixels). During stimulus presentation, the monkeys maintained fixation within a 6.1° × 6.1° window centered on a white dot (0.23° × 0.23°) displayed in the center of the screen with a gray background. Inside the scanner, eye movements were monitored at 60 Hz by an MRI-compatible infrared eye tracking system (LiveTrack AV for fMRI v2, Cambridge Research Systems, Rochester, U.K.).

In the visual meridian mapping, I used the standard stimuli to map the cortical representation of the visual field in human and non-human primates (Wandell et al., 2007; Kolster et al., 2014). Around the FP, two checkerboard wedges with 24° angle were flickered in counterphase at 4Hz (i.e., each wedge was replaced every 250 ms) (Figure 2.2C). The combinations of checkerboard colors were black/white, red/green and blue/yellow. The wedges were presented to the right and left of the FP in the horizontal blocks, and above and below the FP in the vertical blocks. The duration of each block was 16 s. The horizontal and vertical blocks were alternately presented throughout the entire period of each MRI run (272 s) (Horizontal: 9 blocks, Vertical: 8 blocks). As in the training outside the scanner, the monkey received liquid rewards for successful fixation to the FP. Continuous fixation shortened the inter-reward intervals to motivate longer stable fixation.

2.2.8. FMRI data preprocessing

Acquired EPI images were processed using the Functional MRI of the Brain (FMRIB) Software Library (FSL; https://fsl.fmrib.ox.ac.uk/fsl/fslwiki; Smith et al., 2004) and SPM12 software (The Wellcome Centre for Human Neuroimaging; https://www.fil.ion.ucl.ac.uk/spm/; Ashburner, 2012). Initially, using volumes acquired at PE = P/A, FSL's topup processing was applied to all experimental EPI volumes (taken at PE = A/P) to correct for susceptibility induced distortions (Andersson et al., 2003). EPI volumes were then preprocessed using SPM12 as follows: (1) slice timing correction; (2) realignment for compensation for head motions using the first volume as a reference; (3) spatial smoothing by a Gaussian kernel with a 2.0-mm full-width at half maximum. Coregistration processing was applied to the anatomical T1 image and the averaged image of realigned EPI volumes, and the activation maps were overlaid on the T1 image.

2.2.9. Functional image analysis

Statistical analysis of brain activation was performed by SPM12. The activation of each voxel was modeled by a general linear model (GLM) with the standard hemodynamic response function (HRF) implemented in SPM12. I used the following regressors: (1) Horizontal wedge presentation period; (2) Vertical wedge; (3) Reward; (4) Saccade; (5) Blink. Additionally, 6 covariates modeling head movements were also included as nuisance regressors. I defined saccades as eye movements with a maximum velocity exceeding 80°/s. The onset and offset of a saccade were defined as the points at which eye velocity exceeded and fell below 40°/s, respectively. These criteria were determined based on previous studies (Berg et al., 2009; Ito et al., 2013). I defined blinks as periods during which either the pupil center or corneal reflection (the two measures used for the detection of eye movement) could not be detected. Among these periods, I regarded those of less than 50 ms as not blinks but rather as a momentary lapse in detection. This is because completion of an eye blink usually takes more than 100 ms (Goldstein et al., 1992; Tada et al., 2013). The eye-position data in these momentary lapses were linearly interpolated.

Each regressor was a convolution of the HRF with a boxcar-model that took the value of 1 during the occurrence of each event and 0 otherwise. *T*-tests were applied to the estimated GLM's parameters of each voxel, and I defined the voxels that exceeded the threshold of $p < 0.005$ (corrected by family-wise error cluster level correction; FWEc) as significantly activated voxels. Inflated and flattened maps of brain activation were generated for each monkey by Caret5 (https://www.nitrc.org/projects/caret/; Van Essen et al., 2001).

2.2.10. Movement estimation

Movement of monkey's head during scans was estimated by the "realignment" function in SPM12. For each volume, the realignment function estimated the values of translation and rotation relative to the first volume of each run. I call these values "cumulative movements" which represent the displacement of the image position at each time point relative to that in the first volume in each run. I also calculated

the spatial displacement between two consecutive EPI images (taken every 2.0 s) and call these values "relative movements". To quantitatively assess the stability of head restraint, I constructed relative frequency histograms of the relative movements in the three monkeys used in this study (Figure 2.4C–E). I fitted these histograms to a gamma distribution function, with mode and SD used as measures of central tendency and variability, respectively. This is because the histograms in Figure 2.4C–E were substantially positively skewed, and therefore it was not appropriate to use the mean as a representative value (measure of central tendency) for these datasets (i.e., it is not appropriate to fit Gaussian models). Rather, the shape of the graph seemed to be best fit by a gamma distribution function. There are two parameters in a gamma distribution: shape parameter k and scale parameter θ. For gamma distributions with a small k value, the mode rather than the mean is considered to be a more appropriate measure of central tendency. Note that the median of a gamma distribution, as a function of its shape parameter k, has no known representation in terms of elementary functions (i.e., the median cannot be calculated using a simple function). In the present case, because the obtained k values were small, I chose the mode as a measure of central tendency. The standard deviation (SD) in gamma distributions is calculated as $\sqrt{k}\,\theta$.

2.3. Results

2.3.1. Progress of pre-scan training

Training was conducted in a step-by-step manner. Of the three monkeys, I report the progress of monkeys R and T, who underwent a similar, pre-planned training regimen that was developed based on my experience with monkey B (the first monkey used in this study). For monkey B, pre-scan training lasted about 9 months. This period was focused on the optimization of various experimental elements, including optimization of the shape of the plastic mask, stimulus presentation and eye movement measurements in the scanner.

Both monkeys R and T learned the fixation task (continuous fixation for 2–4 min) quickly (monkey R, 42 sessions, about 9 weeks; monkey T, 26 sessions, about 6 weeks) from the start of training with head-restraint (Figure 2.2A,B). The monkeys were then trained on the visual meridian mapping task (Figure 2.2C) and the visual eccentricity mapping task. Again, both monkeys learned these two tasks quickly; the monkeys learned to continue to gaze at the fixation point for more than 90% of the intervals in one block (usually 4–5 min), while localizer stimuli were presented continuously. After training of the visual localizer tasks was complete, I began fMRI data acquisition.

2.3.2. Examination of fMRI data quality

I assessed the quality of the fMRI images obtained with the plastic mask (Figure 2.3, termed "plastic mask monkey"). For comparison, I examined fMRI images of a monkey whose head was restrained by a standard PEEK head-post. The head-post was attached to the skull by PEEK bone screws and dental cement (Figure 2.3, "head-post monkey"). The fMRI images of this monkey were obtained in a different experiment prior to the present study in my laboratory. The images of this head-post-restrained monkey

showed highly noticeable signal drops and distortions near the cortical surface (Figure 2.3A, red and cyan arrows). Although it is not the focus of this paper to determine what exactly caused these signal drops, visual inspection of these EPI images suggests that the adverse effects caused by the implant appear to originate mainly from bone screws; the BOLD signal was affected only near the bone screw holes in this monkey (Figure 2.3B, right). These signal drops can prevent the fine-grained examination of brain activation near the cortical surface. Here, I do not intend to suggest that the head-post implant always has a negative effect on the BOLD signal. For example, the noise from the bone screw may be resolved by ensuring that the drill stops at the inner table of the skull when drilling the hole for the bone screw, and this may allow experimenters to obtain clean EPI images near the brain surface. However, this requires highly-advanced skills and a careful surgery. With the present method, because the plastic mask does not damage the skin or the skull at all, experimenters do not need to be highly skilled in surgical techniques. As shown in Figure 2.3A left, with the plastic mask, there was no change in local magnetic susceptibility, and accordingly there were no signal drops or distortions near the cortical surface.

2.3.3. Examination of head movements

Next, I examined whether or not head movements during a fMRI scan were sufficiently suppressed by the plastic mask. Figure 2.4A,B shows a representative example of the time-course of cumulative head movements in an experimental run which was calculated as the deviation from the first image obtained in this run (see Materials and Methods). These data were collected in the meridian mapping task in monkey B. The magnitude of head movements was estimated by the "realignment" function in SPM12. In Figure 2.4A, the red, blue and green lines indicate translational movements in millimeters along superior-inferior (S-I), right-left (R-L) and anterior-posterior (A-P) axis, respectively. In Figure 2.4B, the red, blue and green lines indicate estimated rotational movements in degrees (pitch, yaw and roll, respectively). The result showed that, for this experimental run, the cumulative movements were successfully suppressed to almost within 0.4 mm (translation) and 0.006° (rotation), except for a single occasion at around 245 s where A-P translational movement showed a spike of about 1.0 mm. According to my observation during the actual scan, this abrupt movement was caused by a large bodily movement accompanying a change in posture.

To confirm that the above result reflects an overall trend across animals, I examined the magnitude of relative movement (Materials and Methods) in the three monkeys while they performed the meridian mapping task (19 runs in 4 sessions in monkey T; 7 runs in 2 sessions in monkey B; 3 runs in 1 session in monkey R; each run lasted 272 s). Figure 2.4C–E shows relative frequency histograms of the estimated relative movements in the three monkeys, with a best-fit gamma distribution function (red curve). The ordinate and abscissa illustrate relative frequency (%) and the magnitude of relative movement (mm), respectively. The results show that in all of the three monkeys, relative movement of greater than 1.0 mm scarcely occurred; the frequencies of such movement were 0.00%, 0.32% and 0.74% in monkeys T, B and R, respectively. Here, the frequency was defined as the percentage of the relative movements exceeding 1 mm out of the total number of relative movement values (i.e., total

number of volumes recorded across all sessions minus one). For example, in monkey T, there were a total of 2,565 relative movement values obtained in 19 runs. The resultant value of 0.00% in monkey T indicates that there were no two consecutive volumes that exhibited relative movements of greater than 1.0 mm across all of the 19 runs in this monkey. The mode values (i.e., the magnitude of the most frequent relative movement) given by the best-fit gamma distribution function were 0.027, 0.032 and 0.055 mm, and the standard deviations were 0.028, 0.025 and 0.046 mm for monkeys T, B and R, respectively.

There have been various studies on the effects of head movements in fMRI (Friston et al., 1996). In many cases, movements within about the size of a voxel (1.5 mm in the present study) were regarded as acceptable (Czisch, et al., 2004; Zou, et al., 2008). Thus, the present results indicate that the plastic mask achieved a sufficient degree of head immobilization for clean fMRI data acquisition in awake monkeys, though during the course of fMRI scans, I noticed that there was a slight difference in the degree of immobilization among the three monkeys. Specifically, in earlier sessions, monkey T tended to show large head movements. For this monkey, I further examined whether its head movements could be better controlled by some remedial measures.

I made two changes and assessed the effect of these changes: a change in the material used to make the mask and a change in the position of the drinking spout. Figure 2.4F–H illustrates changes in the frequency of relative movement over the entire experimental period in each monkey. In each panel, the data in a horizontal row illustrate a relative frequency histogram of relative movement in one run. As I noted above, monkey T showed somewhat frequent head movements in early runs (Figure 2.4F, up to about the 50th run). This was likely caused by a habit of this monkey to make frequent jaw movements upon receiving rewards from the spout. Thus, I decided to increase the strength of the mask material and adjust the position of the spout. A green dotted line in the results of monkey T (between runs 54 and 55) indicates the timing when I remade the mask by using more solid material for better stability (see Materials and Methods). I also took extra care to fit the new material as tight as possible around the zygomatic bones and the occipital ridge.

A yellow dotted line (between runs 98 and 99) indicates the timing when, through trial-and-error and visual inspection, I found the optimal position of the drinking spout where monkey T appeared to show the least jaw movements associated with drinking. The results showed that these modifications had positive effects. Regarding the change in the mask material, although some adjustment period (runs 55–64) was required for the monkey to get used to a new, stiffer mask, compared to the old mask, the new mask reduced the mode and SD values of relative movement from 0.14 to 0.064 mm and from 0.16 mm to 0.074 mm, respectively (data are from runs 45–54 for the old mask and runs 70–79 for the new mask). Subsequently, optimization of the spout position further reduced head movements. Between before and after optimization, the mode and SD values changed from 0.095 to 0.048 mm and from 0.12 to 0.056 mm, respectively (data are from runs 89–98 before optimization, and runs 99–108 after optimization).

For monkey B (Figure 2.4G, green dotted line), although this monkey did not have a head movement issue, I remade the mask for a better fit to achieve a greater degree of head immobilization. For this monkey, I did not change the material used to create the mask. Between before and after the remake (runs 37–46 and 47–56, respectively), the mode and SD values changed from 0.11 to 0.039 mm and from 0.12 to 0.057 mm, respectively. This improvement is clearly visible in Figure 2.4G. These results suggest that, for monkeys that move their heads frequently, the size and frequency of head movements can be reduced by either changing the mask material to increase its rigidity or adjusting factors other than the mask (spout position in the present case) or both.

Since the monkeys certainly would have become more acclimatized to the fMRI environment after each session, not only the remake of the mask and the adjustment of the spout position, but also a training effect should have contributed to the substantial improvement in head stability observed in Figure 2.4F,G. Therefore, I suggest that the improvement of head stability can be ascribed to a combination of three factors: 1) a mask that fits better on the zygomatic bones and occipital ridge, 2) adjustment of the position of the drinking spout, and 3) a training effect.

2.3.4. Retinotopic mapping

To examine whether high-quality fMRI data can actually be obtained by the present method, in each of the three monkeys used in this study, I mapped the borders of the early visual areas (V1–V3) by independent visual stimulation of vertical and horizontal meridians (Rajimehr & Tootell, 2009; Kubilius et al., 2011; Lafer-Sousa & Conway, 2013) (Materials and Methods).

Significant retinotopic responses evoked by a pair of checkerboard wedges are shown in Figure 2.5A,B. The cold colormap represents a vertical meridian and the warm colormap represents a horizontal meridian (Monkey B, left hemisphere, cluster-corrected *t*-statistic map, $p < 0.005$, FWEc). The result clearly reproduces the well-known symmetric retinotopic representations of the quadrant visual field in each of the early visual areas; the vertical wedge stimuli activated the boundaries of V1 and V2, and V3 and V4. The horizontal stimuli activated the boundary of V2 and V3, and the areas in V1. This result was obtained in 19, 7 and 3 experimental runs for monkeys T, B and R, i.e., the same runs that were used in the motion analysis in Figure 2.4D.

Figure 2.5C shows the time-course of *z*-score normalized BOLD signals in one representative voxel within a cluster at the V1/V2 border which was activated by vertical wedges (blue arrow in Figure 2.5B, left). The result showed that the signal strength of this voxel increased, with some hemodynamic delay, after every onset of a vertical wedge and decreased after every change to a horizontal wedge. In contrast, in Figure 2.5D, the exactly opposite pattern of BOLD signal alternations was observed for a voxel within a cluster of V2/V3 border (yellow arrow in Figure 2.5B, right). Comparable results were obtained for other voxels within these clusters.

Figure 2.5E–G shows retinotopic responses overlayed on the flattened occipital cortices of the three monkeys. Although there were some differences in the intensity of activity among the monkeys, the patterns of neural responses to vertical and horizontal wedges revealed the boundaries of each region

of early visual cortices. These results were comparable to those in a prior study in monkeys using a standard head-post method (Lafer-Sousa & Conway, 2013; Kolster et al., 2014).

Regarding the stability of fixation behavior during the meridian mapping task, Figure 2.6B illustrates the distributions of gaze positions in a representative session, in which 7 consecutive runs of the meridian mapping task were performed (monkey T, total scan time = 32 min). Although I used a 6.1° × 6.1° fixation window in this session, I could recalculate, for each run, the percentage of time during which the gaze fell within a smaller imaginary 2.0° × 2.0° fixation window, which is typically used in vison neuroscience studies. The results showed that, in this representative session, this percentage always exceeded 96% in all of the seven runs except for the first run (94.6%). In this analysis, the center of the imaginary 2.0° × 2.0° window was slightly shifted rightward, (x, y) = (0.4°, 0°), relative to the screen center to match the peak of the distributions of gaze positions of this monkey. This is because this monkey has developed a habit of gazing at the right edge of the FP over the course of the experiment. Therefore, I calculated the peak of the gaze distribution during fixation across all sessions and used this value as the center of the imaginary 2.0° × 2.0° fixation window. Because the purpose of this analysis is to check for the stability of fixation, it should not be a problem to slightly shift the position of the imaginary fixation window according to the monkey's habit.

Similar trends were observed across all sessions in the three monkeys that were used to generate brain activity maps in Figure 2.5E–G (19, 7 and 3 runs were conducted in monkeys T, B and R, respectively). The percentage of time during which the gaze position fell within the imaginary 2.0° × 2.0° window was 95.4 ± 1.2 %, 93.7 ± 2.4 % and 84.5 ± 2.3 % in monkeys T, B and R, respectively (mean ± SD). In monkeys B and R, relative to the FP, the center of the imaginary 2.0° × 2.0° fixation window was slightly shifted: (x, y) = (0.6°, 0°), and (x, y) = (0.4°, −0.8°), respectively. These results indicate that, in the present method, problems of instability in eye measurement (e.g., drift or sudden jump of gaze position beyond several degrees caused by a loose head restraint) did not occur.

2.3.5. Upper limit of scan duration using masks

In the present report, the average scan duration across all sessions in the three monkeys (148 sessions) was 19.6 ± 7.4 min. (mean ± SD). The reason why I did not usually scan my monkeys longer than 30 minutes was not because the plastic mask cannot provide strong head-restraint for more than 30 minutes. Rather, this was because I wanted to terminate the scan before even a slight trend in the increase of body and head movement became evident. As is widely known, repeatedly terminating the experiment after the monkeys had begun to move would have reinforced the association that movement would allow them to return to the cage, which in turn would reinforce their body movements in the scanner. I hoped to avoid this from happening in my experiments. In addition, I usually scanned several monkeys in one session. Despite the relatively short scan duration for each monkey, I performed many sessions to obtain a total measurement time.

However, to further support the usefulness of the present method for scans of at least an hour, I selected three sessions, from the longest to the third longest, and assessed if the plastic mask could withstand being worn for 30–60 minutes without showing even a slight trend in the increase of head

movements. These three sessions were a session comprised of 7 consecutive runs of the meridian mapping task (272 s/run, total scan duration = 32 min) (termed “Session 1”, Figures 2.6A and 2.7A), a session comprised of 9 consecutive runs in the free-viewing task with natural movie clips (360 s/run, total scan duration = 54 min) (termed “Session 2”, Figure 2.7B), and a session comprised of 6 runs of the free-viewing task (360 s/run) and 4 runs of a continuous fixation task (272 s/run) with various visual stimuli presented in the periphery (total scan duration = 54 min) (termed “Session 3”, Figure 2.7C). Session 1 is the same session in which the eye movement data shown in Figure 2.6B were obtained.

As shown in Figure 2.6A, in Session 1, throughout the seven runs of the meridian mapping task, the monkey’s head was kept highly stable, with cumulative translational movements well below 0.50 mm in all of the seven runs. Notably, the quality of the head restraint was not deteriorated at all in the seventh run, indicating that there was no increasing trend in the frequency of head movements after 30 minutes of continuous fixation performance. If I consider the head-restraint situation on the final, 7th run, it is likely that scanning could have continued for a few more runs. Summary data for these 7 runs are shown in Figure 2.7A as a relative frequency histogram of relative head movements (the same format as in Figure 2.4C–E). This histogram had a mode value of 0.029 mm and a positively-skewed tail showing an almost complete absence of relative head movements greater than 0.20 mm throughout the session, which indicates that the plastic mask can tightly restrain a monkeys’ head for scans longer than 30 minutes.

The results in Sessions 2 and 3 further supported this view. Figure 2.7B,C shows, from left to right, relative frequency histograms of head movements for the first, second and final 3 or 4 runs (18 min each) in Sessions 2 and 3 (Figure 2.7B, and C, respectively). In both sessions, the three histograms corresponding to the first, second and final 3 or 4 runs are almost identical in shape, with mode values of 0.026 mm, 0.027 mm and 0.026 mm for Session 2 and 0.027 mm, 0.035 mm and 0.030 mm for Session 3. Again, head movements greater than 0.20 mm were almost completely absent in both sessions, which confirmed that there were no signs of deterioration in head stability throughout these 54-min scans. Together, these results suggest that the present method is suitable for functional scans of up to at least an hour.

2.4. Discussion

Use of a commercially available, standard thermoplastic splint material enabled us to easily make form-fitted masks for effective head restraint of monkeys during a fMRI scan. Compared to existing standard invasive methods using a head-post and dental cement, the present method has several advantages: 1) the plastic mask is easy to make (no surgery required) and the shape of the mask can be somewhat changed afterward to improve fit and effectiveness; 2) there is no risk of infection after installation; 3) the monkey's skull and scalp are kept in a completely intact state, allowing measurements to be made without interference from implants to the signal; 4) minimal chair modifications are required to install the mask; in the present report, I only needed to add four screw holes; 5) the cost and time required to implement this method are both low.

Two to three ready-to-use plastic masks can be made within a single anesthesia session (about 30–40 min), without any invasive procedures (Figure 2.1A–G). Because no post-operative recovery period is required, researchers can proceed to the next step (fitting of the mask and chair training under head restraint) within a few days after the mask is made. Through trial-and-error, I identified two critical locations on the skull for optimal head restraint during a fMRI scan: the zygomatic bones and the occipital ridge (Figure 2.1H, arrows). If the mask does not fit well in these areas after it has been made, it is still possible to improve the fit of the existing mask by heating the area with a soldering iron to melt only that part of the mask and then reshaping it or attaching a new piece of softened material. In standard fMRI experiments in awake monkeys, researchers use a non-magnetic head-post to restrain head movements. This invasive technique has the risk of infection at the area of contact between skin and dental cement, as well as around anchor bolts implanted on the skull. The present technique requires no invasive procedures and no chronically implanted materials, resulting in no risk of infection. The present approach improves 'refinement' of the 3R's in animal research by minimizing the monkey's pain and distress.

In previous studies, plastic masks similar to ours have been used in monkeys in neurophysiological recording and transcranial magnetic stimulation (Drucker et al., 2015). In addition, in several previous neurophysiological studies from our group (Kadohisa et al., 2020; Watanabe et al., 2023; Stroud et al., 2023), I have collected both spiking and LFP data using plastic masks that were made of the exact same material used here (i.e., the same model number from the same company). Therefore, after the fMRI measurements, one should be able to move on to neuronal recording experiments by simply cutting the area where the chamber will be implanted with scissors, taking into account the amount of dental cement around the chamber.

In one report on fMRI methodology in monkeys, a plastic helmet was combined with suction of the monkey's scalp (Srihasam et al., 2010). Suction of the scalp was applied through two holes made on both sides of the helmet to achieve further stabilization. Although this helmet showed good head-restraint performance, comparable to that in the standard head-post method, it appears to be a lot of work to create this helmet, including the preparation and maintenance of the suction mechanism. In the present study, I extended these previous results and demonstrated that, if the plastic mask is correctly shaped at a few key areas around the head (i.e., the zygomatic bones and the occipital ridge, Figure 2.1H), it can by itself sufficiently suppress the monkey's head movements in awake fMRI scans. Thus, the present plastic mask has the advantages of being inexpensive, easy to make, and simple to mount on monkeys in daily sessions, requiring only about a minute at most. Another advantage is that the mask does not limit coil-shape options (Figure 2.1I).

Nevertheless, the present technique has at least two limitations. First, as I noted above, although I have demonstrated that the present method is suitable for functional scans of up to at least an hour, I have not tried scans much longer than an hour. Thus, additional studies will be needed to determine whether the plastic mask can be used in fMRI experiments using a contrast agent such as monocrystalline iron-oxide nanoparticles (MION) (Vanduffel, et al., 2001), which usually last several

hours. Second, head movements induced by changes in body posture or those that the monkey intentionally makes of its own volition are difficult to suppress using this mask. According to my observation, such head movements are sometimes greater than 1 mm. However, if the monkey used in an experiment does not often show these behaviors, this should not be a critical issue. In fact, in the present study, my monkeys rarely showed such large, abrupt head movements even without any special, additional training to reduce body movements during a scan. In the present study, head movements greater than 1 mm were limited to less than 1.1% of the number of volumes recorded in the latest 30 runs for the three monkeys (Figure 2.4F–H). Certainly, the present method is ineffective for monkeys who have a habit of moving their bodies frequently in the scanner, and for monkeys that do not like head restraint and do not stop resisting, but this issue also applies to a standard head-post. To conclude, the present, easy-to-make plastic mask has a strong potential to simplify fMRI experiments in awake monkeys, while the obtained data are as good as or even better quality than those with the conventional head-post method.

2.5. Figures

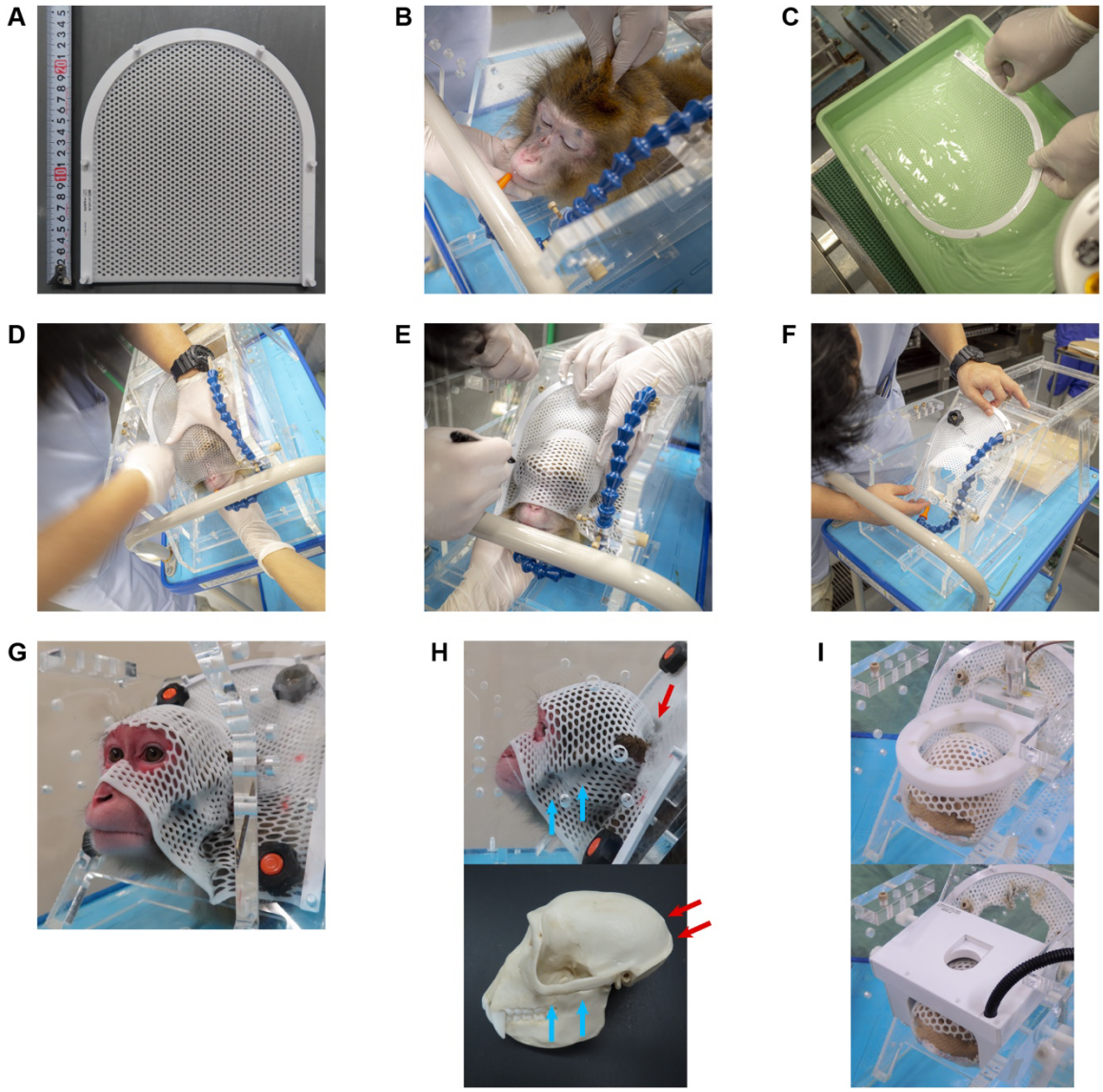

Figure 2.1. Mask preparation procedure.

(A) Plastic splint material used to make a mask. (B) The head of an anaesthetized monkey was set in the same position as in the usual experiment. (C) Splint material immersed in hot water (> 90°C). (D) The moment when the softened splint material was pressed against the monkey's head after cooling (< 50°C). Note that one person grasped the monkey's jaw and tried to keep the monkey's head still, while the other person shaped the splint material. (E) Cutting lines drawn by a permanent marker. (F) The mask was attached to a chair using M6 screws to check its compatibility with the chair. (G) Front view of a monkey restrained by the plastic mask. (H) Side view of a monkey (top) and a model of the corresponding scalp (bottom). Note that in the good mask, the splint material was bent to perfectly conform to the shapes of the zygomatic bones (cyan arrows) and the occipital ridge (red arrows). (I) Two types of receiver coils used in the present study. By making the shape of the mask closely fit the monkey's head, various types of coils could be placed close to the monkey's head.

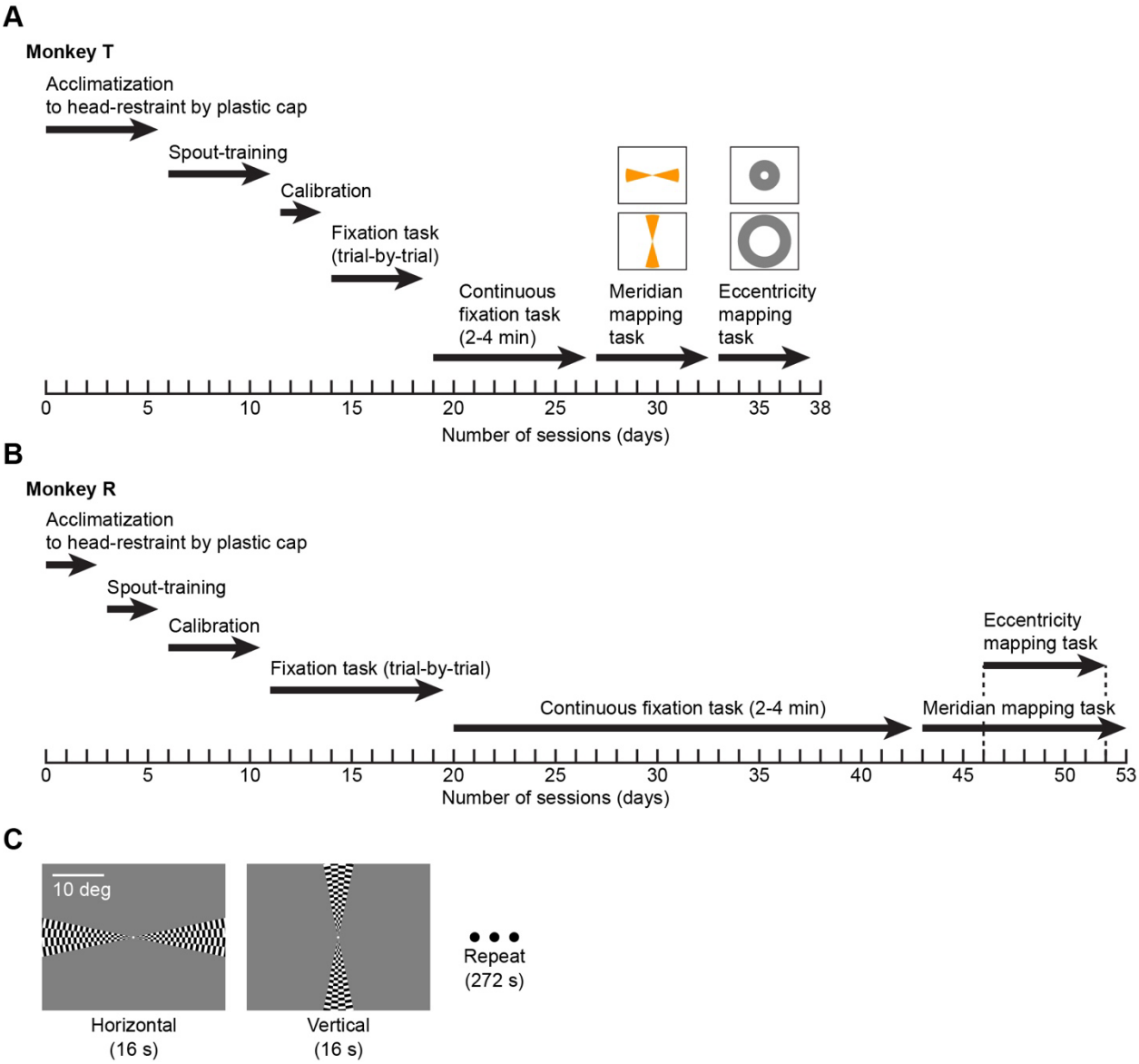

Figure 2.2. Step-by-step training regimen in pre-scan training.

(A) Progress of pre-scan training in monkey T. (B) Same as in A, but for monkey R. (C) The visual stimuli for the horizontal and vertical meridian mapping. In the actual experiments, chromatic checkerboard (red/green and blue/yellow) patterns were also presented. A scale bar indicates visual angle.

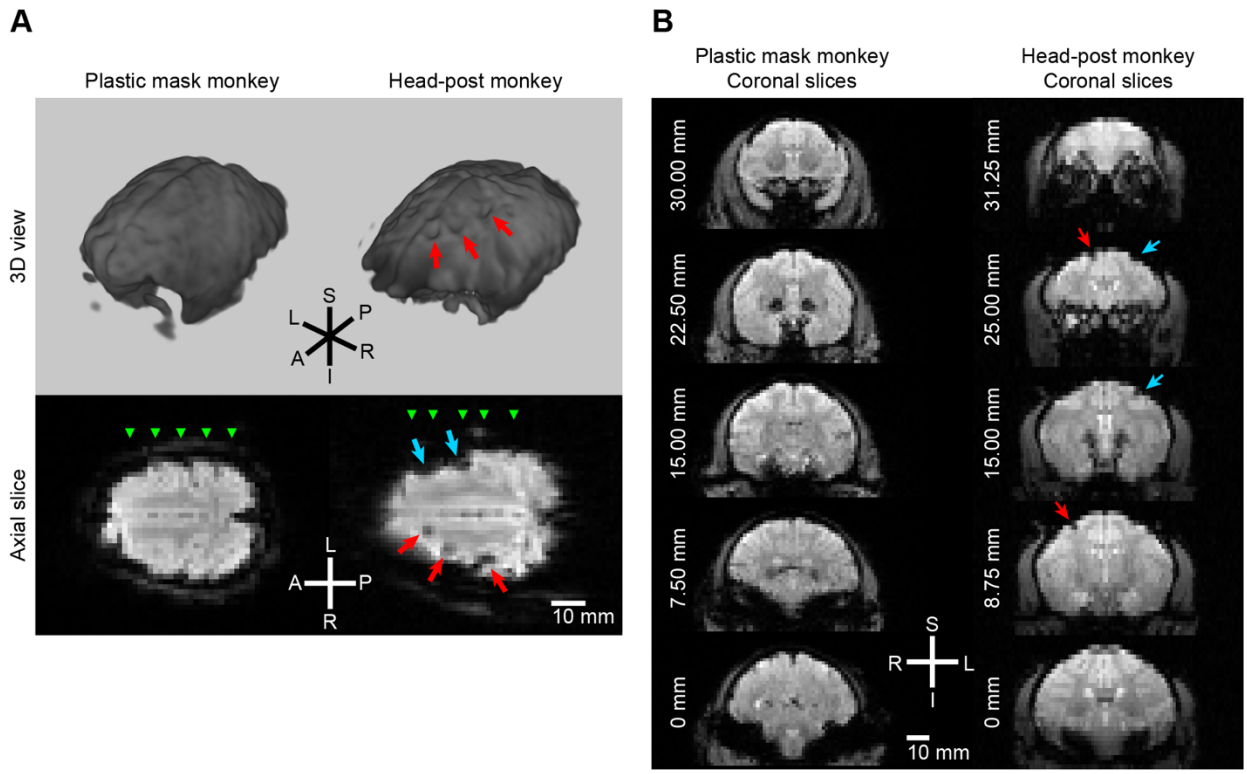

Figure 2.3. Comparison of EPI images between the plastic mask and the head-post methods.

(A) The upper row shows 3D views of the brains reconstructed from EPI data. Left, data acquired with a plastic mask (monkey B, termed 'plastic mask monkey'). Right, data acquired with a head-post (monkey K, termed 'head-post monkey'). The bottom panels show axial slices 6.4 mm below the vertex in each monkey. Red and cyan arrows indicate signal drop near bone screw holes. Green triangles indicate AP positions of the slices presented in B. (B) Coronal slices of the two monkeys shown in **A**. The numbers on the left represent the distance from the most posterior slice of the five images for each monkey.

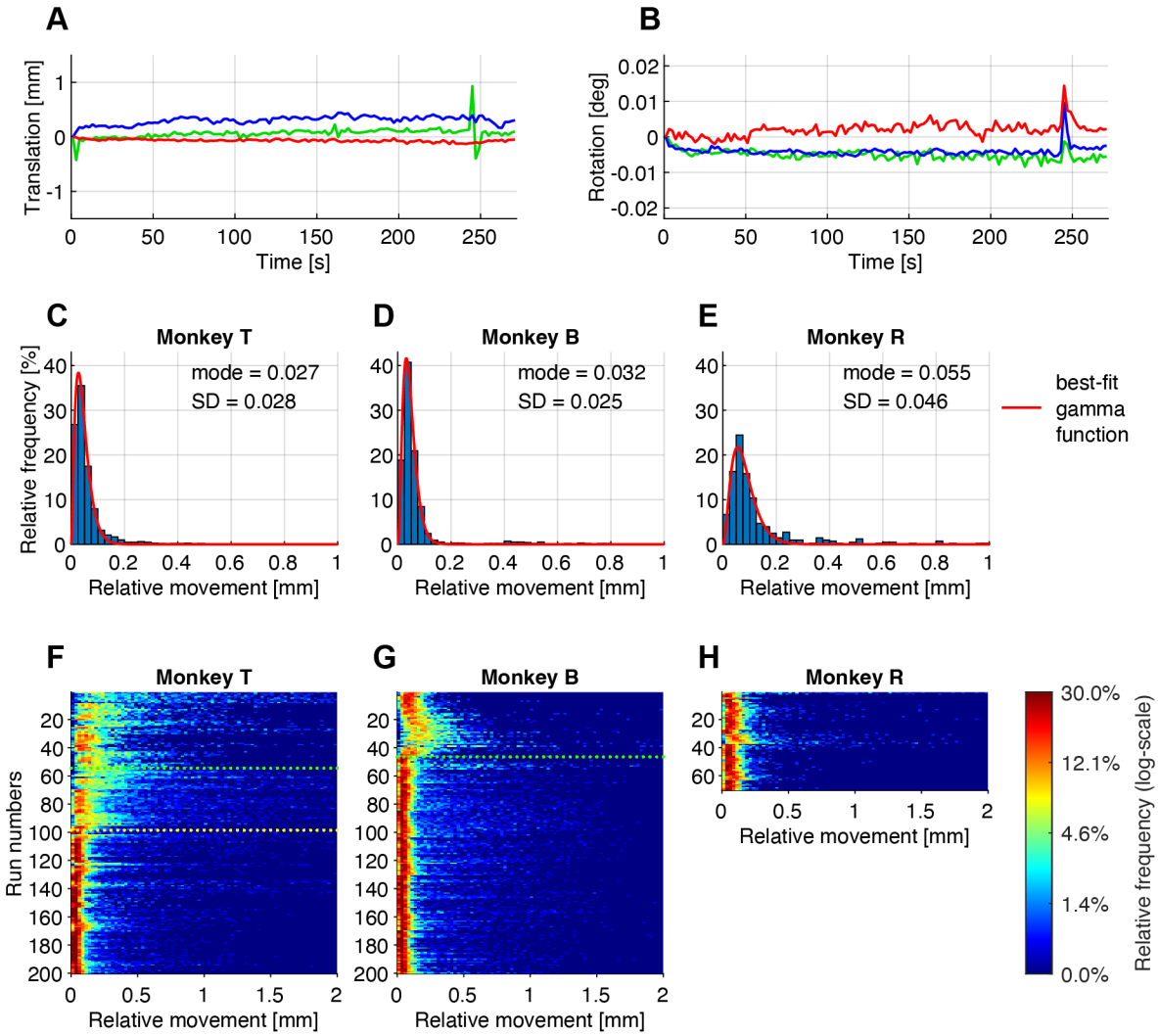

Figure 2.4. Head movements during fMRI scans.

(A) Example of cumulative translational movements of the brain in millimeters in monkey B. Red, blue and green lines indicate the movements along the right-left, superior-inferior and anterior-posterior axes, respectively. The data were obtained during a single run of the meridian mapping task. (B) Same as in A, but for cumulative rotational movements in degrees. (C–E) Relative frequency histograms of relative movements (bin width = 0.025 mm) in each monkey during the meridian mapping task. The data were from the latest 19, 7 and 3 runs in monkey T, B and R, respectively. Red curves indicate gamma distribution function fit to each histogram, with peak point (mode) and standard deviation (SD) values. (F–H) Longitudinal record of the relative movement of individual monkeys throughout the experiment. The data in each horizontal row indicate a relative frequency histogram of relative movement in one run shown as a log-scale color map. The data are ordered from the first run (top of panels) to the last run (bottom). The data were obtained from all experimental runs in which monkeys were engaged either in continuous fixation (272 s/run, including the visual meridian task) or in free-viewing of movie clips of various natural scenes (300 or 360 s/run). Green dotted lines in monkeys T and B indicate the timing when I reshaped the mask for an improved fit to the zygomatic bones and the occipital ridges. For monkey T, I also changed the material of the mask to a more solid one. The yellow dotted line in monkey

T indicates the timing when I adjusted the spout position. Runs that were interrupted due to hardware problems or the monkey's maladaptive behavior were excluded.

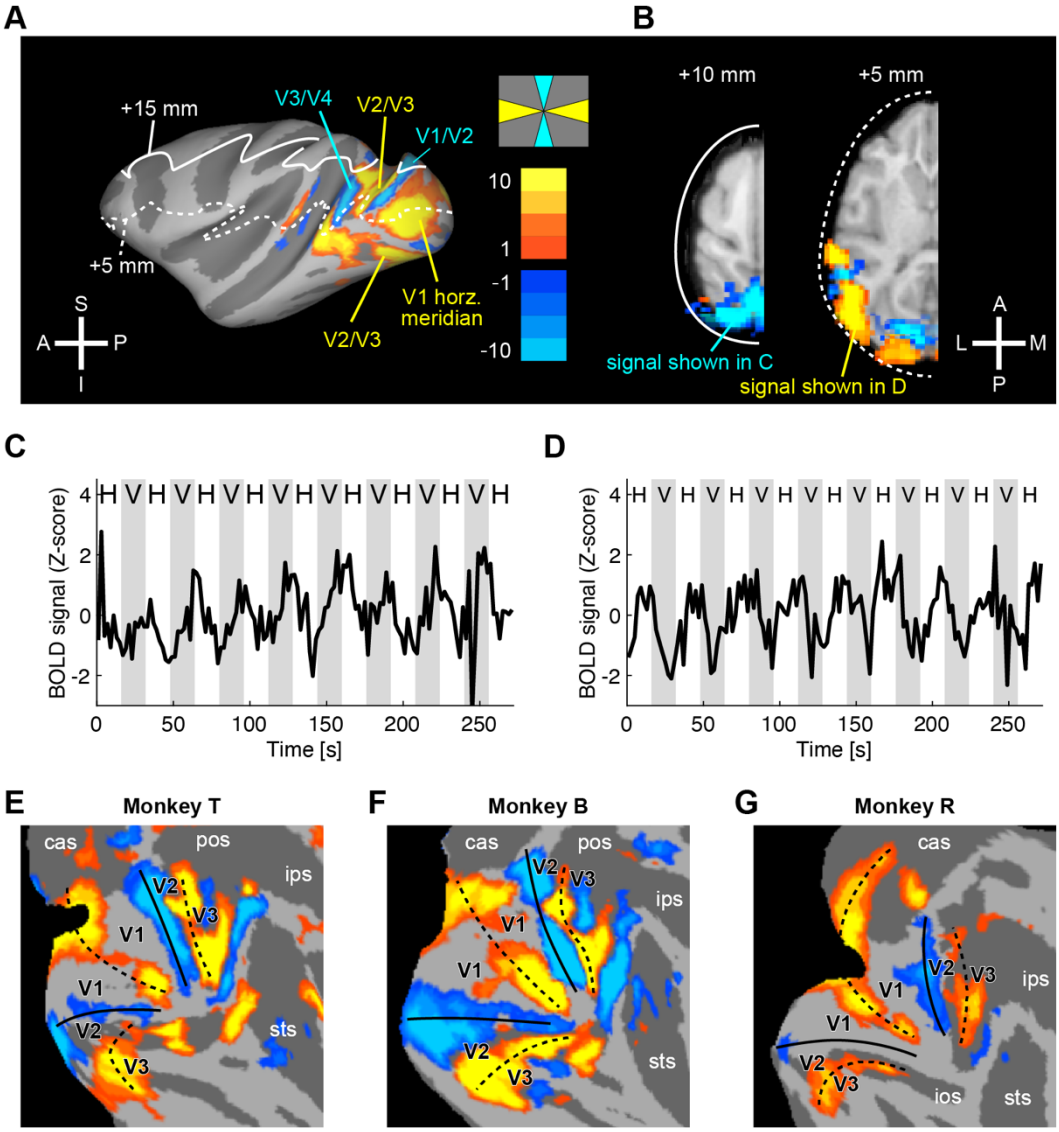

Figure 2.5. Activation of the borders of early visual cortices.
(A) Cluster-corrected *t*-statistics map of voxels that were significantly activated by either the vertical (cold colors) or horizontal (warm colors) wedges ($p < 0.005$, FWEc) overlayed on the cortical surface. Two white lines indicate the positions of axial slices shown in B (+15 mm and +5 mm slices relative to the AC-PC plane. (B) Axial slices of the left hemisphere taken at the levels shown in A. (C) Time-course of BOLD signal modulation in one representative voxel taken from the cluster shown in the left panel in B. The cluster was activated by vertical wedges. The background colors of the plot area correspond to the orientations of wedges presented during that period (white: horizontal wedge, 'H'; gray: vertical wedge, 'V'). (D) Same as in C, but for a voxel taken from the cluster shown in the right panel in B which was activated by the horizontal wedges. (E–G) Flat map display of brain areas in individual monkeys that were significantly activated by the wedges (right hemisphere, $p < 0.005$, FWEc). The

color codes were the same as in **A**. The dashed and solid black lines indicate the estimated borders of visual areas.

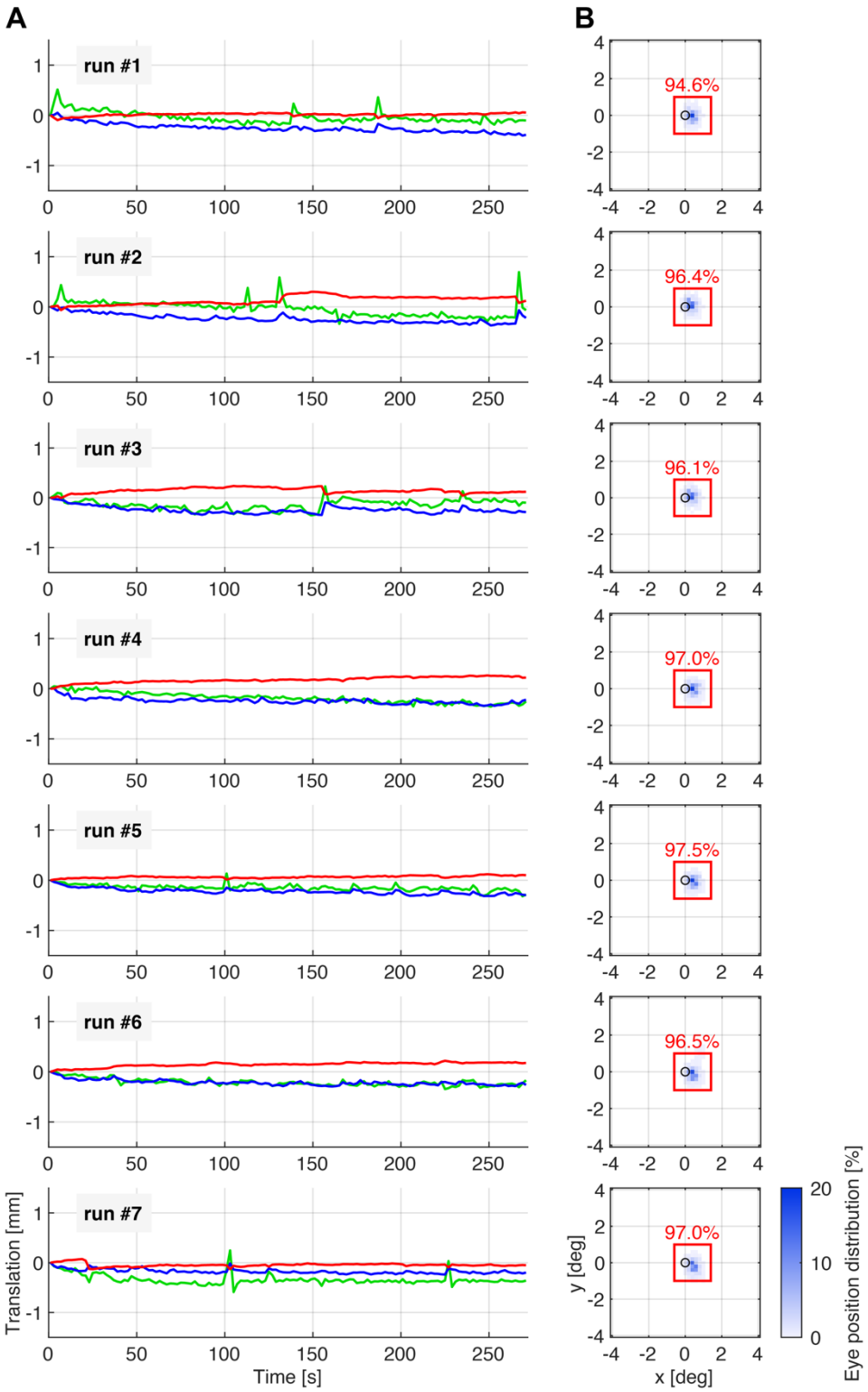

Figure 2.6. Head movements and fixation performance for 7 consecutive runs in monkey T.

(A) Cumulative translational movements of the brain in each run. Each row corresponds to the result from the first to the seventh run of the session. Other conventions as in Figure 2.4A. (B) Distribution of

eye position during the performance of continuous fixation in the meridian mapping task. Each row corresponds to the result from the first to the seventh run. The ordinate and abscissa indicate the distance from the center of the screen (and FP). The unfilled black circle indicates the exact size and location of the FP. The red square indicates the imaginary 2.0° × 2.0° fixation window which was shifted slightly to the right to compensate for the monkey's gazing habits. Numbers above the red square indicate the percentage of time out of the entire duration of each run (272 s) during which eye position fell within the imaginary 2.0° × 2.0° fixation window.

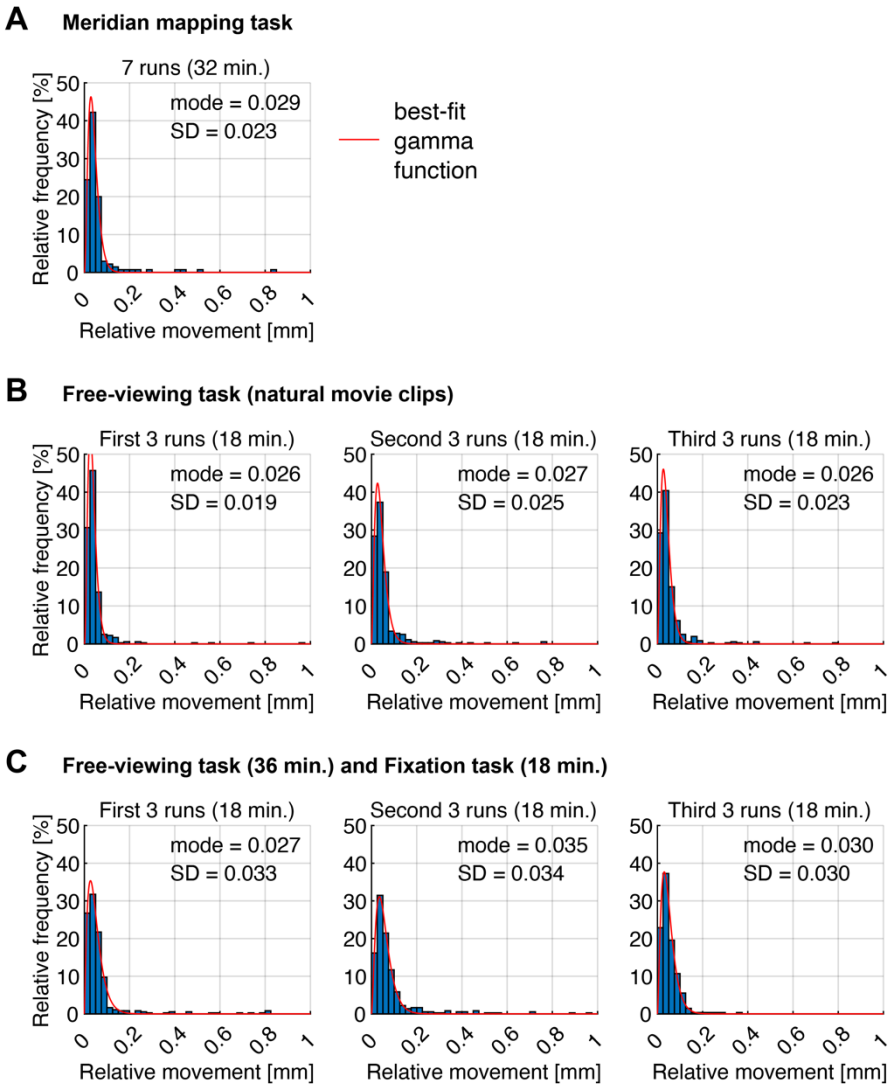

Figure 2.7. Stability of head-restraint in a long session.

(A) Relative frequency histograms of relative movements of monkey T during the meridian mapping task (Session 1). The data come from all of the 7 runs shown in Figure 2.6. Conventions as in Figure 2.4C–E. (B) Same as in A, but for Session 2, which was comprised of 9 runs of the free-viewing task (300 s/run × 9 runs = 54 min). Left, middle and right panels indicate the results in the first, second and final 3 runs of this session (18 min each). (C) Same as in B, but for Session 3, which was comprised of

6 runs of the free-viewing task (360 s/run) and then 4 runs of the continuous fixation task (272 s/run) with various visual stimuli presented in the periphery (total scan time = 54 min).

2.6. References

Andersson, J. L., Skare, S., & Ashburner, J. (2003). How to correct susceptibility distortions in spin-echo echo-planar images: application to diffusion tensor imaging. NeuroImage, 20(2), 870-888.

Ashburner, J. (2012). SPM: A history. *NeuroImage*, 62(2), 791-800.

Berg, D. J., Boehnke, S. E., Marino, R. A., Munoz, D. P., & Itti, L. (2009). Free viewing of dynamic stimuli by humans and monkeys. *J. Vis.*, 9(5), 1-15.

Czisch, M., Wehrle, R., Kaufmann, C., Wetter, T. C., Holsboer, F., Pollmächer, T., & Auer, D. P. (2004). Functional MRI during sleep: BOLD signal decreases and their electrophysiological correlates. *Eur. J. Neurosci.*, 20(2), 565-574.

Drucker, C. B., Carlson, M. L., Toda, K., DeWind, N. K., & Platt, M. L. (2015). Non-invasive primate head restraint using thermoplastic masks. *J. Neurosci. Methods*, 253, 90-100.

Friston, K. J., Williams, S., Howard, R., Frackowiak, R. S., & Turner, R. (1996). Movement-Related effects in fMRI time-series. *Magn. Reson. Med.*, 35(3), 346-355.

Goldstein, R., Bauer, L. O., & Stern, J. A. (1992). Effect of task difficulty and interstimulus interval on blink parameters. *Int. J. Psychophysiol.*, 13(2), 111-117.

Ito, J., Maldonaldo, P., & Grün, S. (2013). Cross-frequency interaction of the eye-movement related LFP signals in V1 of freely viewing monkeys. *Front. Syst. Neurosci.*, 7, 1-11.

Kadohisa, M., Watanabe, K., Kusunoki, M., Buckley, M. J., & Duncan, J. (2020). Focused Representation of Successive Task Episodes in Frontal and Parietal Cortex. *Cereb. Cortex*, 30(3), 1779-1796.

Kolster, H., Janssens, T., Orban, G. A., & Vanduffel, W. (2014). The Retinotopic Organization of Macaque Occipitotemporal Cortex Anterior to V4 and Caudoventral to the Middle Temporal (MT) Cluster. *J. Neurosci.*, 34(31), 10168-10191.

Ku, S.-P., Tolias, A. S., Logothetis, N. K., & Goense, J. (2011). fMRI of the Face-Processing Network in the Ventral Temporal Lobe of Awake and Anesthetized Macaques. *Neuron*, 70(2), 352-362.

Kubilius, J., Wagemans, J., & Op de Beeck, H. (2011). Emergence of perceptual Gestalts in the human visual cortex: the case of the configural-superiority effect. *Psychol. Sci.*, 22(10), 1296-1303.

Lafer-Sousa, R., & Conway, B. R. (2013). Parallel, multi-stage processing of colors, faces and shapes in macaque inferior temporal cortex. *Nat. Neurosci.*, 16(12), 1870-1878.

Logothetis, N. K., Guggenberger, H., Peled, S., & Pauls, J. (1999). Functional imaging of the monkey brain. *Nat. Neurosci.*, 2(6), 555-562.

Miyamoto, K., Osada, T., Setsuie, R., Takeda, M., Tamura, K., Adachi, Y., & Miyashita, Y. (2017). Causal neural network of metamemory for retrospection in primates. *Science*, 355(6321), 188-193.

Oritz-Rios, M., Haag, M., Balezeau, F., Frey, S., Thiele, A., Murphy, K., & Schmid, M. C. (2018). Improved methods for MRI-compatible implants in nonhuman primates. *J. Neurosci. Methods*, 308, 377-389.

Rajimehr, R., & Tootell, R. B. (2009). Does Retinotopy Influence Cortical Folding in Primate Visual Cortex? *J. Neurosci.*, 29(36), 11149-11152.

Smith, S. M., Jenkinson, M., Woolish, M. W., Beckmann, C. F., Behrens, T. E., Johansen-Berg, H., . . . Zhang, Y. (2004). Advances in functional and structural MR image analysis and implementation as FSL. *NeuroImage*, 23, S208-S219.

Srihasam, K., Sullivan, K., Savage, T., & Livingstone, M. S. (2010). Noninvasive functional MRI in alert monkeys. *NeuroImage*, 51, 267-273.

Stroud, J. P., Watanabe, K., Suzuki, T., Stokes, M. G., & Lengyel, M. (2023). Optimal information loading into working memory in prefrontal cortex explains dynamic coding. *PNAS*.

Tada, H., Omori, Y., Hirokawa, K., Ohira, H., & Tomonaga, M. (2013). Eye-Blink Behaviors in 71 Species of Primates. *PLos One*, 8(5), 1-9.

Van Essen, D. C., Drury, H. A., Dickson, J., Harwell, J., Hanlon, D., & Anderson, C. H. (2001). An Integrated Software Suite for Surface-based Analyses of Cerebral Cortex. *J. Am. Med. Inform.*

Assoc., 8(5), 443-459.
Vanduffel, W., Fize, D., Mandeville, J. B., Nelissen, K., Hecke, P. V., Rosen, B. R., . . . Orban, G. A. (2001). Visual Motion Processing Investigated Using Contrast Agent-Enhanced fMRI in Awake Behaving Monkeys. *Neuron*, 32(4), 565-577.
Wandell, B. A., Dumoulin, S. O., & Brewer, A. A. (2007). Visual field maps in human cortex. *Neuron*, 56(2), 366-383.
Watanabe, K., Kadohisa, M., Kusunoki, M., Buckley, M. J., & Duncan, J. (2023). Cycles of goal silencing and reactivation underlie complex problem-solving in primate frontal and parietal cortex. *Nat. Commun.*, 14, 5054.
Zou, Q.-H., Zhu, C.-Z., Yang, Y., Zou, X.-N., Long, X.-Y., Cao, Q.-J., . . . Zang, Y.-F. (2008). An improved approach to detection of amplitude of low-frequency fluctuation (ALFF) for resting-state fMRI: Fractional ALFF. *J. Neurosci. Methods*, 172(1), 137-141.

Chapter 3
Neural Bases for Discriminating the Temporal Direction of Time's Arrow: An Awake Monkey fMRI Study

3.1. Introduction

We perceive time as unidirectional: it flows from the past into the present and proceeds toward the future. Guided by this belief, humans are constantly predicting future events in an ever-changing environment, adjusting their perception of the external stimuli, and preparing forthcoming actions. Indeed, in experimental psychology, it is well-established that humans can judge the temporal order of two successive stimuli even when they are separated by only 20–30 ms (Hirsh & Sherrick, 1961; Pöppel, 1997). Nevertheless, there is substantial evidence demonstrating that this ability is remarkably flexible. For example, attention (Duncan et al., 1997) and prior experiences (Friston, 2012; Knill & Pouget, 2004) can alter temporal judgments, such that two simultaneous stimuli are perceived as occurring sequentially (Hikosaka et al., 1993; Shore et al., 2001), or two stimuli separated by 20–80 ms are perceived as occurring simultaneously (Fujisaki et al., 2004; Miyazaki et al., 2006; Sugita & Suzuki, 2003). Moreover, our group and other teams have previously demonstrated that subjective temporal order of tactile stimulations can be easily reversed by simply crossing one's hands, with subjective reversal of the correct stimulation order occurring at stimulus separations of up to 100–500 ms (Heed & Azañón, 2014; Shore et al., 2002; Yamamoto & Kitazawa, 2001). These findings highlight that perception of time flow is highly malleable; even the direction of time's arrow is not as fixed as we tend to believe, despite our conviction that any reversal would be "nonsensical."

In a recent behavioral study, our group investigated the mechanisms that enable humans to discriminate the direction of time's arrow by presenting 360 video clips of diverse natural scenes in either forward or reverse playback. Participants made speeded judgments about the playback direction. Somewhat surprisingly, they erred on 39% of trials when the video was played in reverse (i.e., incorrectly judging reverse playback as forward), while they erred on only 9% of trials for forward-replayed videos. Closer inspection revealed that, in some videos (66/360) containing certain "cues" (i.e., forward motion, free fall, diffusion, and division/addition), participants could accurately detect reverse playback, and responded more rapidly and in greater unison than when judging forward replay. Thus, clear violations of physical plausibility by these cues appear to trigger a prediction-error detection mechanism, giving rise to the perception of the reversal of time's arrow. Subsequent human fMRI data from our group revealed that the right middle temporal gyrus (MTG) and the left cerebellum showed stronger responses to reverse- than forward-replayed videos (Hanyu et al., 2023b, conference presentation; article in preparation). Given that the cerebellum is known to compare predicted sensory states (derived from motor commands) with actual sensory input and detect mismatches, these findings

suggest that a similar prediction-error mechanism involving the cerebellum may be engaged when individuals detect “nonsensical” or unexpected motion in the environment. Additionally. another group has reported that the superior temporal sulcus and temporo-occipital junction showed selectively activation to forward biological motion in a human fMRI study (Maffei et al., 2015).

Based on these observations in humans, the present study employed fMRI in awake monkeys to examine whether a homologous neural mechanism is involved in monkey time-flow perception. If so, this would pave the way for future electrophysiological investigations to clarify the underlying neuronal circuits in more detail. Previous pioneering electrophysiological work in monkeys demonstrated that neurons in the anterior superior temporal sulcus (aSTS) respond more strongly to forward than reverse presentations of biological motion (Oram & Perrett, 1994, 1996). These results suggest that the monkeys brains also possesse specialized neural circuitry for discriminating the temporal flow of visual stimuli.

Here, I expand on that research by presenting both biological and non-biological motion sequences in forward and reverse playback, measuring whole-brain activity via fMRI (Experiment 1). This approach enabled us to determine whether brain regions beyond the aSTS are sensitive to time-flow direction. To distinguish time-flow selectivity from other forms of visual plausibility, I performed a control measurement in which monkeys viewed normal (upright) videos and their vertically flipped (inverted) counterparts (Experiment 2). By comparing these two conditions, I sought to delineate the brain regions selective for the direction of time flow in the scene and those selective for the spatial orientation of the scene, and to determine whether these areas respond specifically to the temporal plausibility of motions or to the overall physical plausibility (i.e., spatiotemporal coherence) of motions.

3.2. Methods and Materials

3.2.1. Subjects

I used two female Japanese monkeys (Macaca fuscata): monkey A (7 years old, 6 kg) and monkey B (5 years old, 6 kg). Prior to this study, both monkeys participated in another fMRI experiment in which I trained them to enable fMRI data acquisition using head fixation with a non-invasive plastic mask (Chapter 2; Tanaka et al., 2024). During the experiment, the monkeys sat quietly in a sphinx position within an MRI-compatible acrylic monkey chair (UMI Inc., Kyoto). Their head movement was restrained using a custom-fitted mask made of thermoplastic splint material (product numbers: MTAPUR or MTAPUIR2232, CIVCO Radiotherapy, Orange City, IA). Both monkeys were trained in various eye movement tasks, including fixation and saccade tasks, which facilitated the calibration of eye movements and ensured accurate gaze position measurement. For the present experiment, the monkeys were trained to watch short natural video clips (3–5 seconds) presented on a screen. While the monkeys looked within the displayed video frame, they were randomly rewarded with juice at intervals of 1–2 seconds, encouraging them to watch the videos. Interestingly, even without rewards, the monkeys appeared highly engaged with the videos, showing strong interest in prominent elements such as characters’ faces or key objects within the scenes. All training was conducted in a mock scanner environment. FMRI data acquisition began after the monkeys’ gaze stayed within the boundaries of the

displayed video frame for at least an average of 90% of the playback time across all clips in a session. The experimental procedures were approved by the Animal Research Committee at the Graduate School of Frontier Biosciences, Osaka University, and were in full compliance with the guidelines of the National BioResource Project "Japanese Macaques" and the National Institutes of Health guide for the care and use of Laboratory animals.

3.2.2. Visual stimuli

In the MRI scanner, visual stimuli were back-projected onto a screen positioned 56 cm in front of the monkeys' faces (Figure 3.1A). The screen covered a visual field of 34.7° × 28.2° (1280 × 1024 pixels) and had a gray background. Video clips were presented at the center of the screen within a region subtending 21.8° × 21.3°. Visual stimuli were presented by Psychtoolbox (http://psychtoolbox.org/) in MATLAB (MathWorks, Natick, MA, USA). The monkeys were allowed to view the stimuli freely. Eye movements were recorded at 60 Hz using an MRI-compatible infrared eye camera (LiveTrack AV for fMRI v2, Cambridge Research Systems, Rochester, U.K.). To maintain motivation during data acquisition, fruit juice rewards were delivered at random intervals, typically every 6–11 s.

A total of 619 videos were selected for presentation, including 419 biological motion clips and 200 non-biological motion clips (Figure 3.1E) drawn from the 'Moments in Time Dataset' (Monfort et al., 2020) and the 'StoryBlocks database' (https://www.storyblocks.com/). Because the present study focused on brain activity that selectively represents the correct temporal flow or spatial orientation of natural scenes, and because a previous human behavioral study, which was conducted in our laboratory, demonstrated that forward and falling motions of both animated and non-animated objects strongly cue the perception of temporal direction (Hanyu et al., 2023a), I selected videos specifically featuring such motions for this experiment. Each selected clip originally varied in length, so a 3-second segment (90 frames at 30 frames per second, fps) was extracted to capture the period with the most prominent motion. In some cases, multiple non-overlapping 3-second segments were extracted from a single video.

The present study consisted of Experiments 1 and 2, with the selected clips presented differently in each experiment as described below. In Experiment 1, trials involved presenting a single video clip either in its original forward playback direction (forward trials) or reversed in time (reverse trials) (Figure 3.1B). Each trial began with a 1-second static display of the video's first frame, followed by a 3-second presentation of the video clip (forward or reverse), then a 1-second static display of the final frame, and concluded with a 4–6 second blank interval on a gray background (Figure 3.1D). Forward and reverse trials were presented in randomized order. In total, 2,476 trials were conducted over 75 runs, spanning 24 sessions for monkey A and 23 sessions for monkey B, with each video shown twice in the forward condition and twice in the reverse condition within this period.

Experiment 2 consisted of trials in which the videos were presented in either their original upright orientation (upright trials) or an upside-down, spatially inverted orientation (inverted trials) (Figure 3.1C). Of the 419 biological motion videos used, 219 were presented once in each orientation (upright and inverted), while the remaining 200 biological motion videos, along with the 200 non-biological motion videos, were presented twice in each orientation throughout the experiment. In total,

2,038 trials were conducted over 61 runs, spanning 17 sessions for monkey A and 20 sessions for monkey B.

3.2.3. MR data acquisition

The blood oxygen level-dependent (BOLD) signals were acquired using echo-planar imaging (EPI) method on a 3T Magnetom Prisma-Fit MRI scanner (Siemens, München, Germany). The monkey's head was immobilized in the monkey chair using a custom-made plastic mask, and a custom-built 12-channel phased-array receiver coil (Takashima Seisakusho Co., Ltd., Tokyo, Japan) was placed around this mask, ensuring complete coverage of the brain. Each daily session typically comprised four functional scans (hereafter referred to as "runs"), with each run lasting 300 or 360 seconds. The imaging parameters for these runs were as follows: TR = 1 s, TE = 30 ms, flip angle = 60°, matrix size = 86 × 86, isotropic voxel size = 1.5 mm, 45 slices, and an anterior-to-posterior (A/P) phase encoding direction (PE). To enable distortion correction via topup processing, 10 additional EPI images were acquired with a reversed (P/A) phase encoding direction in each session (day).

In a separate session, T1-weighted anatomical images of higher spatial resolution were obtained under anesthesia (medetomidine: 0.03 mg/kg, i.m.; midazolam: 0.2 mg/kg, i.m.; and butorphanol tartrate: 0.3 mg/kg, i.m.). A single-channel loop coil (Takashima Seisakusho Co., Ltd.) was employed, and the imaging parameters for these anatomical scans were: TR = 1.5 s, TE = 1.92 ms, flip angle = 8°, matrix size = 192 × 192, voxel size = 0.67 mm isotropic, and 192 slices. Six anatomical scans were collected for monkey A and four for monkey B, after which the respective datasets were averaged to improve the signal-to-noise ratio. The activation maps, that is the results of analyzing functional images, are displayed on this averaged T1-weighted anatomical image of each monkey in this paper.

3.2.4. FMRI data preprocessing

All acquired EPI datasets were preprocessed with the FMRIB Software Library (FSL; https://fsl.fmrib.ox.ac.uk/fsl/fslwiki) (Smith et al., 2004), SPM12 (The Wellcome Centre for Human Neuroimaging; https://www.fil.ion.ucl.ac.uk/spm/) (Ashburner, 2012), Caret5 (https://www.nitrc.org/projects/caret/) (Van Essen et al., 2001), and MATLAB. Susceptibility-induced distortions were corrected by employing FSL's topup algorithm (Andersson et al., 2003), which utilized reference volumes collected with PE = P/A and applied the resulting corrections to the experimental EPI volumes acquired with PE = A/P (Figure 3.2A). Subsequent preprocessing steps were performed in SPM12. These included (1) realignment of all EPI volumes to the first volume to mitigate head motion effects (motion correction), and (2) spatial smoothing using a Gaussian kernel with a full-width at half maximum (FWHM) of 2.0 mm. Following these procedures, the T1-weighted anatomical image (motion-corrected and averaged across multiple scan runs) was coregistered to the average of the realigned EPI images (Figure 3.2B). This alignment allowed for visualization of activation maps overlaid onto the corresponding anatomical T1 image. The surface map of each monkey's brain was generated from the averaged T1-weighted anatomical image using the Caret5 software (Figure 3.2C).

3.2.5. Functional image analysis

Statistical analyses of brain activity were performed using SPM12. I modeled each voxel's activity in each run with a general linear model (GLM) defined as followed:

$$y = X\beta + \epsilon \quad (1)$$

where y is the voxel-wise time-series BOLD signal; X is the regressor matrix (with each column corresponding to a specific regressor); β denotes the vector of estimated coefficients, and ϵ indicates the residual error. The following regressors were included in the GLM: (x_1) motion energy; (x_2) forward (Experiment 1) or upright (Experiment 2) biological motion; (x_3) reverse (Experiment 1) or inverted (Experiment 2) biological motion; (x_4) forward (Experiment 1) or upright (Experiment 2) non-biological motion; (x_5) reverse (Experiment 1) or inverted (Experiment 2) non-biological motion; (x_6) blank; (x_7) reward; (x_8) saccade; and (x_9) blink. Additionally, six nuisance regressors modeling head motion parameters were included. Each regressor was generated by convolving the macaque-specific hemodynamic response function (HRF) (Leite et al., 2002), with a boxcar function set to 1 during each event and 0 otherwise. The motion energy regressor was computed using the MATLAB codes provided in a previous study (Nishimoto et al., 2011), transformed to a logarithmic scale, and convolved with the HRF. The head motion regressor was used without convolution. A voxel-wise estimation of the beta coefficient (β_i) for each regressor (x_i) was performed using SPM12.

Saccades were defined as eye movements with peak velocities exceeding 80°/s, with their onsets and offsets identified when eye velocity surpassed or fell below 40°/s, respectively (Berg et al., 2009; Ito et al., 2013). Blinks were defined as periods during which the pupil center or corneal reflection (the two measures used to track eye movements) could not be detected. Given that blinks typically last around 100 ms (Goldstein et al., 1992; Tada et al., 2013), detection gaps shorter than 50 ms were not classified as blinks. Eye-position data during these brief lapses were linearly interpolated.

The estimated beta values of the GLM across all runs were subjected to *t*-tests to identify regions with significant activation. I focused the following three contrasts:

$$\text{Fwd}\gtrless\text{Rev (Upr}\gtrless\text{Inv) contrast (All):} \quad \beta_2 + \beta_4 \gtrless \beta_3 + \beta_5 \quad (2)$$

$$\text{Fwd}\gtrless\text{Rev (Upr}\gtrless\text{Inv) contrast (Bio):} \quad \beta_2 \gtrless \beta_3 \quad (3)$$

$$\text{Fwd}\gtrless\text{Rev (Upr}\gtrless\text{Inv) contrast (Non-Bio):} \quad \beta_4 \gtrless \beta_5 \quad (4)$$

The voxels that exhibited significant activation in a given contrast were defined as follows. Tasking Experiment 1 as an example, which compared forward and reverse video-playback conditions (hereafter referred to as Forward and Reverse conditions, respectively), regions which exhibited significant responses in the Fwd>Rev contrast (All) were identified through the following steps: (1) voxels showing β_2+β_4 (Forward)>0 responses were masked ($p < 0.05$), (2) among these masked voxels, those showing β_2+β_4 (Forward)>β_3+β_5 (Reverse) responses were selected ($p < 0.005$), and (3) only clusters that met a cluster-level family-wise error (FWE) correction threshold ($p < 0.05$) or contained voxels surpassing a peak-level FWE correction threshold ($p < 0.05$) were considered significant.

3.3. Results

3.3.1. Validation of the non-invasive head-restraint technique

Prior to Experiment 1, I performed a standard retinotopic mapping scans to confirm the compatibility of the non-invasive head-fixation technique (Chapter 2) with fMRI data acquisition and to assess the signal quality (S/N level) for each of the two monkeys (Figure 3.3A). In this procedure, flickering checkerboard stimuli, one along the horizontal and the other along the vertical visual meridian, were alternately presented. By identifying regions exhibiting significant activation to the meridian checkerboard stimuli of a particular orientation, I aimed to delineate the borders of lower visual areas (Figure 3.3B,C). The results showed that while the intended borders were clearly imaged in both monkeys, monkey A's map appeared more distinct than monkey B's, despite both datasets comprising an equal number of volumes (7 runs = about 32 minutes). This difference likely reflects monkey A's excellent in-scanner behavior (i.e., body immobility and attentional engagement), whereas monkey B demonstrated highly proficient in-scanner behavior, albeit slightly less so than monkey A. Thus, in the main results that follow, I focus first on monkey A's data. I then present monkey B's results and compare them to monkey A where relevant.

3.3.2. Experiment 1 (Forward/Reverse)

Figure 3.4A shows clusters in monkey A that exhibited significant responses in the Fwd≧Rev contrast (All). Significant clusters were observed only for the Fwd>Rev contrast (warm colors) and were located in subcortical areas rather than the cerebral cortex: specifically, the right medial pulvinar and the left superior colliculus (SC). The right medial pulvinar had a peak *t*-value of 7.8 and a cluster size of 97 voxels, while the left SC had a peak *t*-value of 4.8 and a cluster size of 2 voxels.

In the Fwd≧Rev contrast (Bio), activation in these two subcortical regions became more prominent (Figure 3.4B, top right panel), merging into a single larger cluster with a peak t-value of 6.8 and a cluster size of 179 voxels. Notably, unlike the previous contrast (i.e., the Fwd≧Rev contrast (All)), significant Forward > Reverse activation emerged in the cerebral cortex. Prominent responses were observed in the middle superior temporal sulci (mSTS) of both hemispheres (LH, peak *t*-value = 5.3, cluster size = 66 voxels; RH, peak *t*-value = 5.0, cluster size = 128 voxels), regions known for detecting biological motion. Additionally, activation was detected in the left lunate sulcus (LUS) (peak *t*-value = 4.7, cluster size = 29 voxels), corresponding to V2. The robust response in mSTS highlights its sensitivity to the "life-like" dynamics inherent in forward motion, while the activation in the LUS suggests that even early visual areas play a role in evaluating the plausibility of biological movement.

Contrary to this Fwd≧Rev contrast (Bio) (which showed no Reverse > Forward response), the Fwd≧Rev contrast (Non-Bio) elicited significant Reverse > Forward activation in the right mSTS (peak *t*-value = 5.0, cluster size = 16 voxels), near the left mSTS (peak *t*-value = 4.9, cluster size = 21 voxels), and in a portion of the cerebellum (peak *t*-value = 4.8, cluster size = 15 voxels) (Figure 3.4C). These findings resemble those obtained in human fMRI experiments conducted in our laboratory (Hanyu et al., 2023b, conference presentation; article in preparation), supporting the proposed model that a

cerebello-cortical prediction-error detection network contributes to playback direction (forward/reverse) judgments.

Figure 3.5A shows the clusters in monkey B that exhibited significant responses in the Fwd≧Rev contrast (All). Similar to monkey A, the clusters detected in monkey B favored Forward over Reverse playback. However, unlike monkey A, in which significant clusters were observed only in subcortical regions (i.e., SC and pulvinar), no subcortical clusters were detected in monkey B. Instead, cortical clusters were identified in the left anterior STS (peak *t*-value = 5.0, cluster size = 45 voxels) and the right middle STS (peak *t*-value = 4.5, cluster size = 183 voxels). The Fwd>Rev contrast (Bio) yielded significant activation in the left anterior STS (peak *t*-value = 4.9, cluster size = 53 voxels) and the right middle STS (peak *t*-value = 4.4, cluster size = 130 voxels) (Figure 3.5B, warm colors). This pattern aligns well with findings in monkey A, in which significant activation was also detected in the right middle STS for the same contrast (Figure 3.4B). This close correspondence between the two monkeys reinforces the view that the STS is sensitive to temporally coherent, life-like motion.

Nevertheless, the significant cluster in the left STS of monkey B is located more anteriorly compared to the left middle STS cluster observed in monkey A (Figure 3.4B). Although the reason for this discrepancy remains unclear, prior single-unit studies have reported forward-motion-selective neuronal activity in the anterior STS (Oram & Perrett, 1994, 1996), near the left anterior STS cluster identified in monkey B. Thus, this anterior STS region, observed exclusively in monkey B, is also likely to preferentially process biological motion with correct temporal order.

The medio-dorsal two voxels of the left SC in monkey A exhibited a forward-preferential response that passed familywise error correction at peak-level (Figure 3.4A,B, Table 1). To assess whether these findings generalize to the other side and to the SC of monkey B, we compared the averaged BOLD signals of the two voxels (Figure 3.6A) with those of their counterparts (Figures 3.6B–D). In the two voxels, the mean BOLD signal increased with two peaks in response to forward replay: one near the end of video replay (4 s) and another approximately 2 s after the offset of the still image (6–7 s). These two peaks were generally observed in the counterpart voxels (Figures 3.6B–D) and were larger in response to forward replay (red curves) than to reverse replay (blue curves). In five of the six counterparts, the difference during the period of the second peak reached significance. These findings suggest that the Forward > Reverse response in the medio-dorsal SC region is a generalizable phenomenon observed in both hemispheres across different monkeys.

In the Fwd≧Rev contrast (Non-Bio), clusters in several distinct regions exhibited differential activations between the Forward and Reverse playback conditions: the right thalamus (Forward > Reverse, peak *t*-value = 5.7, cluster size = 37 voxels), the right calcarine sulcus (CAS) (Forward > Reverse, peak *t*-value = 4.6, cluster size = 152 voxels), and the putamen (Forward > Reverse, peak *t*-value = 5.0, cluster size = 18 voxels) (Figure 3.5C). Notably, the right thalamus was also identified in monkey A under the same contrast (Table 3), though its localization within the thalamus differed: in monkey A, the cluster was located in the posterior region, whereas in monkey B, it was detected in the anterior region.

3.3.3. Experiment 2 (Upright/Inverted)

Figure 3.7A shows clusters in monkey A that exhibited significant responses in the Upr⩾Inv contrast (All). Significant Upright > Inverted activation was primarily observed in the arcuate sulcus (AS) (LH, peak *t*-value = 5.7, cluster size = 31 voxels; RH, peak *t*-value = 5.9, cluster size = 54 voxels), the V2 (peak *t*-value = 9.4, cluster size = 554 voxels) and the STS (LH, peak *t*-value = 9.0, cluster size = 237 voxels; RH, peak *t*-value = 9.3, cluster size = 202 voxels). In the Upr⩾Inv contrast (Bio), these clusters in the STS, V2 and AS remained significant for the Upr>Inv contrast (Figure 3.7B). Notably, restricting the analysis to biological motion (rather than all videos) revealed an even stronger STS response to the upright biological motion (LH, peak *t*-value = 10.6, cluster size = 281 voxels; RH, peak *t*-value = 10.0, cluster size = 381 voxels). This result indicates that the STS preferentially processes biologically plausible motion aligned with the direction of gravity, which corroborates earlier reports that the primate STS exhibits stronger responses to upright than inverted biological motion (Grèzes et al., 2001; Grossman & Blake, 2001; Wang et al., 2022). Together with findings from Experiment 1, which demonstrated stronger bilateral STS activation for forward- compared to reverse-played biological motion, the results observed in monkey A provide compelling evidence that the monkey STS exhibited selectivity for motion aligns spatially and temporally with real-world biological dynamics.

It is worth noting that area V2 also exhibited a significant Upright > Inverted activation under the biological-only contrast. This result indicates that spatial orientation of biological motion is processed early in the visual pathway. Together with the significant Forward > Reverse activation in the right LUS (V2; Figure 3.4B), my findings suggest that even early visual areas contribute to evaluating the plausibility of biological movement (forward and upright vs. reverse and inverted). However, it remains to be determined whether these responses reflect purely bottom-up processing or are influenced by top-down feedback from higher-order regions (e.g., STS).

In the Upr⩾Inv contrast (Non-Bio), significant activation was observed in the LUS (peak *t*-value = 5.0, cluster size = 81 voxels) and the AS (peak *t*-value = 4.5, cluster size = 37 voxels) for the Upright > Inverted contrast (Figure 3.7C). Notably, these regions also exhibited significant activation for the same contrast in the biological-only contrast. This result suggests that the LUS and AS preferentially respond to visual motion aligned with the direction of gravity, irrespective of whether the stimulus involves a biological entity. In contrast, the STS did not show significant activation for the Upr> Inv contrast (Non-Bio), indicating that its preference for gravity-aligned motion may be specific to biological stimuli.

Figure 3.8 shows the activation maps of monkey B. In the Upr⩾Inv contrast (Bio), significant clusters were observed in the bilateral AS (LH, peak *t*-value = 6.2, cluster size = 50 voxels; RH, peak *t*-value = 7.6, cluster size = 93 voxels) and bilateral STS (LH, peak *t*-value = 12.2, cluster size = 212 voxels; RH peak *t*-value = 11.5, cluster size = 218 voxels) (Figure 3.8B, warm colors). Notably, these same regions also showed significant activation in monkey A (Figure 3.7B), which indicates that, in both monkeys, the STS exhibited forward-preferential responses in Experiment 1 and upright-

preferential responses in Experiment 2. Thus, these results confirm that the monkey STS is selective for biological motion presented in the correct temporal direction and the correct spatial orientation.

In the Upr≷Inv contrast (Non-Bio), several regions exhibited distinct activations between the Upright and Inverted playback conditions, including the left putamen (Upright > Inverted, peak *t*-value = 6.2, cluster size = 91 voxels), the right LUS (Inverted > Upright, peak *t*-value = 4.9, cluster size = 69 voxels), and the right rostral superior temporal gyrus (rSTG) (Inverted > Upright, peak *t*-value = 6.2, cluster size = 91 voxels) (Figure 3.8C). However, these findings were not replicated in monkey A, indicating that they may lack robustness.

Cortical regions specific for temporal and spatial processing

We compared cortical distributions of regions revealed in the first (temporal: Fwd > Rev) and the second (spatial: Upr > Inv) experiments (Figure 3.9). In three of the four hemispheres (bilateral hemispheres of Monkey A and the right hemisphere of Monkey B), the time specific region (shown in red) was located posteriorly as compared to the space specific region (shown in blue) that extended along the STS, with a common region in between (shown in yellow) (Figure 3.9A, L21, L19 and R19; Figure 3.9B, R25 and R23). These results suggest that posterior side of the middle STS processes temporal plausibility, while anterior side of the middle STS evaluates the validity of biological motion regardless of temporal or spatial inversion.

Additionally, in both monkeys, the IOS showed distinct distributions of Forward > Reverse and Upright > Inverted responses. Superior regions of the IOS processed Forward > Reverse information, while inferior regions processed Upright > Inverted information (Figure 3.9A, L29, R29, R27 and R25; Figure 3.9B, R29 and R27). This suggests that detection of temporally plausible biological motion occurs early in the visual pathway, possibly influenced by feedback from higher-order regions such as the STS.

Other than the STS and IOS, no overlapping clusters were detected. The Fwd>Rev (Bio) clusters detected in the SC and pulvinar (Figure 3.4B), and the Rev>Fwd (Non-Bio) cluster in the cerebellum of Monkey A (Figure 3.4C) may reflect responses specific to temporal inversion, but further investigation is needed to confirm their robustness.

3.4. Discussion

In this study, I aimed to elucidate the neural substrates underlying discrimination of time's arrow by conducting fMRI measurements in awake monkeys. Using natural short video clips, I manipulated the direction of temporal progression of natural scenes by presenting the videos in both their normal forward direction (Forward) and a temporally reversed direction (Reverse) to examine the influence of playback direction on neural activity (Experiment 1). I found that the monkey STS consistently exhibit stronger responses to forward than to reverse presentations of biological motion (Experiment 1, Figures 3.4B and 3.5B). The superior colliculus (SC) and medial pulvinar also showed forward-preferential responses to biological videos (Figure 3.4B). Comparing regions where showed forward- and upright-preferential

activation revealed that the more posterior side of the middle STS exhibited responses specific to the temporal direction, whereas the anterior portion responded to biologically plausible motions in a broader sense, incorporating both temporal direction and spatial orientation (Figure 3.9). Additionally, in the IOS, distinct regions exhibited responses specific to either temporal or spatial aspects. Together, these results suggest that the monkey STS and IOS are selectively tuned to biological motion that is plausible in both temporal direction and spatial orientation. In particular, the posterior side of the middle STS and the superior side of the IOS, which exhibited responses specific to the temporal direction, are likely to be key regions involved in discriminating the direction of the "time's arrow."

For non-biological motion, regions near the left STS, the right STS, and the right cerebellum showed greater activity during reverse- compared to forward-playback (Figure 3.4C). This pattern may reflect activation of the cortico-cerebellar error-detection network in response to unexpected movements during reverse playback. Together, the present findings suggest that distinct neural pathways for discriminating the temporal direction underlie the processing of biological and non-biological motion. It is likely that forward playback preferentially engages circuits tuned to biologically plausible movement, whereas reverse playback activates error-detection networks that respond to unexpected motions, particularly in non-biological stimuli.

3.4.1. The SC and the STS preferentially detect biological motions that are more physically plausible

In Experiment 1, the left SC, the right medial pulvinar, and bilateral STS exhibited significant Forward > Reverse responses to biological motion (Figures 3.4B and 3.5B). Based on the analysis of averaged BOLD signal in each voxel, the SC in both hemispheres of both monkeys consistently exhibited a forward > reverse response to biological motion (Figure 3.6). A previous study (Lu et al., 2024) demonstrated that both human and monkey SC responds more strongly to upright (i.e., non-inverted) biological motion compared to inverted motion, highlighting the importance of correct spatial orientation in biological motion detection by the SC. Prior anatomical studies in monkeys have documented connections from the SC, via the pulvinar, to the STS (Berman & Wurtz, 2010; Bogadhi et al., 2021). The present Forward > Reverse responses among the SC, pulvinar, and STS expand on these earlier findings and suggest that this subcortical-cortical network is sensitive not only to spatial inversion but also to temporal inversion in biological motion.

3.4.2. Why the GLM analysis failed to fully capture the forward-preferential response in the SC

In the Fwd>Rev contrast (All) and Fwd>Rev contrast (Bio), the SC was detected only in the left hemisphere of monkey A. However, the mean BOLD signal in the SC counterparts revealed similar Fwd>Rev responses in both hemispheres across the two monkeys (Figure 3.6). It is apparent that the temporal profiles of the mean BOLD signal, with the largest peak at 6−7 s after the movie onset, was slower than the standard hemodynamic function used in the GLM analysis of the present study: the standard function, constructed from the HRF of the early visual cortex in macaque monkeys (Leite et

al., 2002), may not accurately capture BOLD responses from the subcortical structures. In Experiment 1 of this study, SC, pulvinar, and cerebellar activations were detected only in monkey A. One possible reason for the limitations is that the responses in these subcortical and cerebellar regions may not have been adequately represented by the HRF of the early visual cortex.

3.4.3. Role of the STS and cerebellum in prediction-error coding during naturalistic motion perception

For non-biological motion videos, the right mSTS, the vicinity of the left mSTS and a portion of the cerebellum exhibited stronger response to reverse than forward playback of non-biological motion videos (Figure 3.4C). These reverse-preferential responses resemble findings from a related human study in our laboratory (Hanyu et al., 2023b, conference presentation; article in preparation). In this study, reverse playback of natural scene video similar to those used in the present study elicited significant activation in the right middle temporal gyrus (MTG) and the left cerebellum, which suggests that a prediction-error detection network, spanning right cortical regions and the left cerebellum, is activated when participants evaluate the direction (forward or reverse) of each video playback. The present results suggest that a comparable network exists in the macaque brain and is particularly engaged in processing non-biological motion, such as falling objects.

3.4.4. Preference of the arcuate sulcus for upright-played videos

A significant preference for upright motion in biological movies was found in the bilateral arcuate sulcus (AS), which accommodates the frontal eye field (FEF) in both monkeys (Figures 3.7B and 3.8B), as well as in the right lateral intraparietal area (LIP) in monkey A (Table 8). The FEF and LIP are interconnected regions that serve as critical nodes for the control of eye movements and the regulation of attention (Balan et al., 2019; Premereur et al., 2014; Wardak et al., 2011). The upright-preferential activations may reflect differences in eye movements arising from the substantial shift in the location of salient objects between upright and inverted videos. In upright biological motion videos, the organism's face, typically the primary focus of overt attention, is positioned near the top of the screen, whereas in the inverted condition, it appears at the bottom, potentially altering gaze patterns. Because inverting biological motion is known to impair face-recognition accuracy (Adachi et al., 2009; Pinsk et al., 2009; Thompson, 1980), less attention may have been directed toward the face in the inverted videos (Balan et al., 2019; Premereur et al., 2014; Wardak et al., 2011). Furthermore, prior works have reported that the focus of attention shifts depending on the walking direction of an animal (Ding et al., 2017; Shi et al., 2010) and that gaze behaviors differ between forward- and reverse-playback of natural videos (Suda & Kitazawa, 2015). Although no temporal-direction–related activations in FEF or LIP were observed in Experiment 1, this may simply reflect the relatively minor effect of reversing temporal orientation – compared to spatial inversion – on eye movements. Therefore, it remains worthwhile to investigate in future studies whether the FEF and LIP might exhibit forward-preferential neural activity.

3.4.5. Conclusion

This study investigated the neural bases underlying the discrimination of time's arrow in non-human primates. Using fMRI, I identified that the superior temporal sulcus (STS), superior colliculus and medial pulvinar selectively respond to forward biological motion. The results suggest that a subcortical-cortical network projecting from the superior colliculus (SC) through the pulvinar to the superior temporal sulcus (STS) encodes plausible temporal dynamics of biological motion. Conversely, for non-biological motion, reverse playback elicited significant activations in the cerebellum and STS. These results suggest that the cerebro-cerebellar network, which works as a prediction-error detector, is involved in identifying unexpected or nonsensical motion.

I identified distinct pathways that discriminate the direction of time's arrow, as indicated by forward-preferential responses to biological motion and reverse-preferential responses to non-biological motion. These findings deepen our understanding of the fundamental mechanisms underlying primate time perception and pave the way for further investigations, such as electrophysiological recordings.

3.5. Figures and Tables

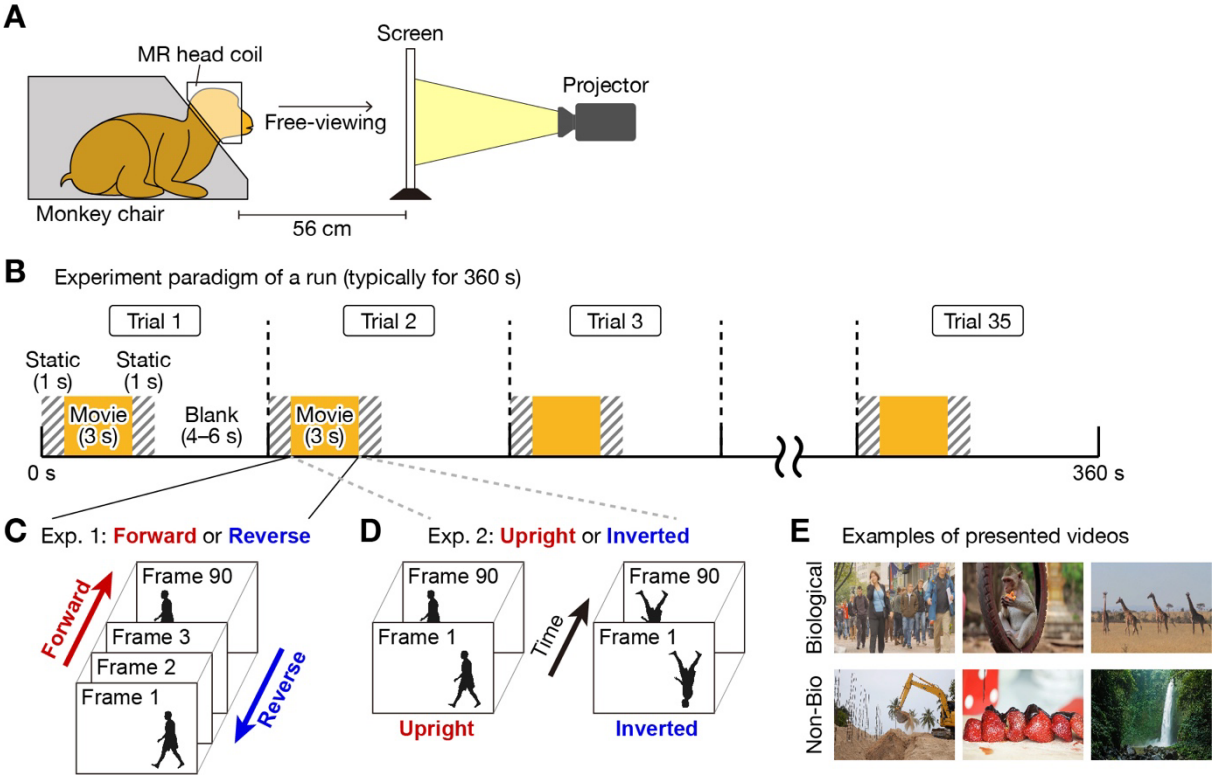

Figure 3.1. Experimental procedures.

(A) Schematic of the setup for the scan inside the scanner. The monkey was seated in a sphinx position in a monkey chair, freely viewing video stimuli back-projected onto a screen positioned 56 cm in front. A half-mirror was placed in front of the monkey's face to allow one eye to be recorded using an eye camera positioned directly above. A nozzle to deliver juice rewards was positioned near the monkey's mouth. (B) Progression of a single run: Each run typically consisted of 35 trials and lasted a total of 360 seconds. Each trial began with a 1-second static display of the first frame of each video clip, which was followed by 3 seconds of video playback. The final frame was then displayed statically for 1 second, after which a blank screen (ITI) appeared for 4–6 seconds before the next trial. (C) Stimulus presentation in Experiment 1. In the forward condition, the video clip was played sequentially from the 1st to the 90th frame, while in the reverse condition, it was played in a temporally reversed order, from the 90th to the 1st frame. The forward and reverse conditions presented randomly on a trial-by-trial basis within each run. (D) Stimulus presentation in Experiment 2. In the upright condition, the video was played in its original orientation, while in the inverted condition, it was played in a spatially flipped (upside-down) orientation. The upright and inverted conditions were presented randomly on a trial-by-trial basis within each run. (E) Examples of videos used in this study: The upper and lower three images show frames from biological motion videos and non-biological motion videos, respectively. A total of 419 biological motion videos and 200 non-biological motion videos were selected from the StoryBlocks and Moments in Time databases.

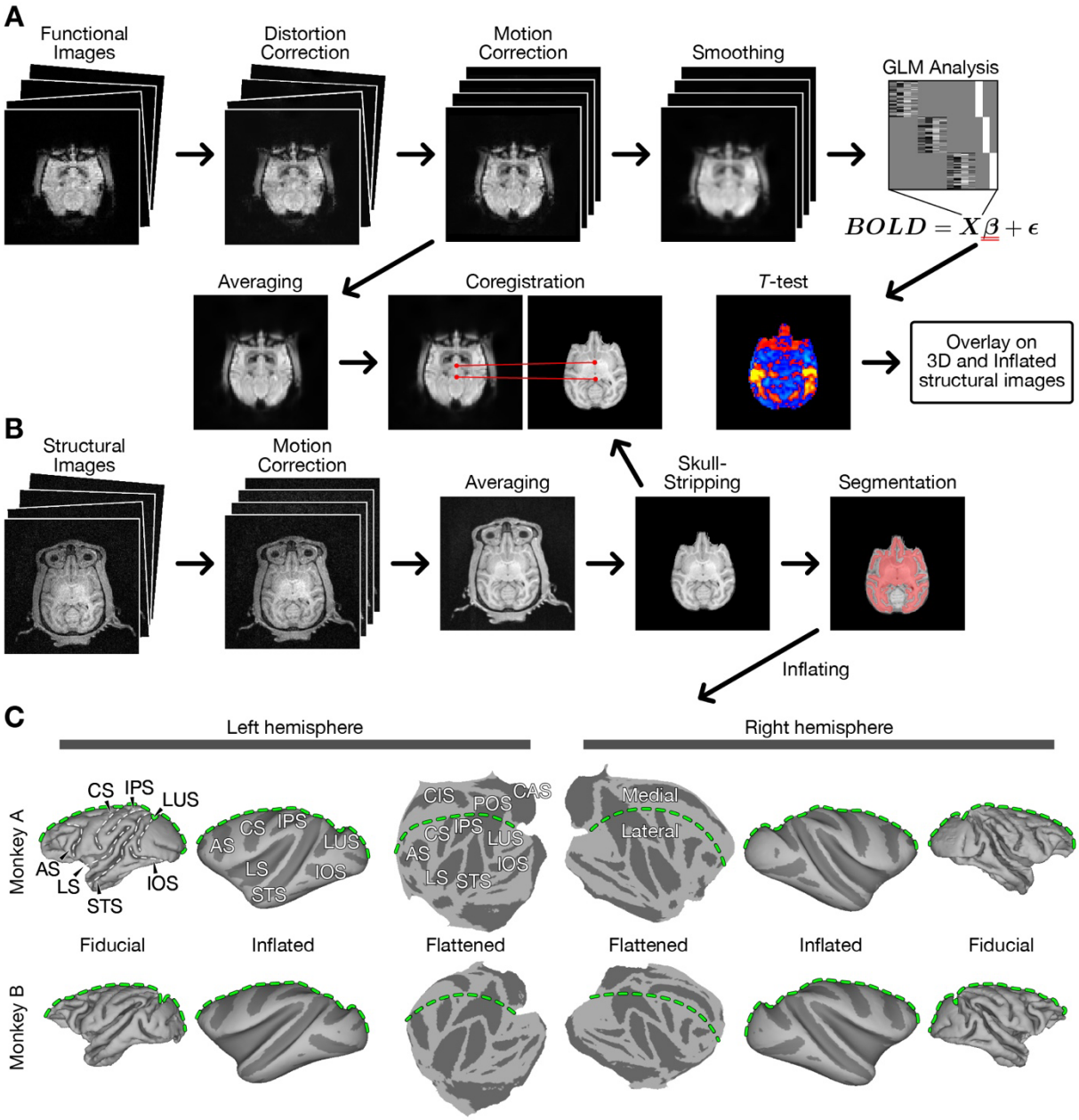

Figure 3.2. Processing pipeline of MRI data.

(A) Processing of the functional images. Susceptibility-induced distortions were first corrected using the topup function in FSL. Motion correction was then applied, and the corrected images were averaged to generate a mean image, which was subsequently coregistered to the structural image. All functional images were smoothed with a Gaussian kernel with a full-width at half maximum (FWHM) of 2.0 mm. Then, a voxel-wise general linear model (GLM) analysis was applied to the data from each run with regressors as described in Methods. The resulting beta values for each regressor, pooled across all runs, were subjected to a *t*-test to evaluate statistical significance. (B) Processing of the structural images. Motion correction was first applied, and the resulting images were then averaged. Next, skull-stripping was performed by creating a mask that separated the brain from the skull, using the drawing tool in Caret5 for manual delineation. The images obtained after skull-stripping were subsequently used for coregistration with the functional images. Finally, white matter and gray matter segmentation was

conducted through an automated intensity-based procedure, followed by manual corrections as needed. (C) Inflated and flattened cortical surfaces of monkeys A (top panels) and B (bottom panels), which were generated by Caret5 using the segmentation masks that separate white and gray matter. The green dashed line indicates the midline (shown as a white dashed line in subsequent figures). AS: arcuate sulcus, CAS: calcarine sulcus, CIS: cingulate sulcus, CS: central sulcus, IOS: inferior occipital sulcus, IPS: intraparietal sulcus, LS: lateral sulcus, LUS: lunate sulcus, POS: parieto-occipital sulcus, STS: superior temporal sulcus.

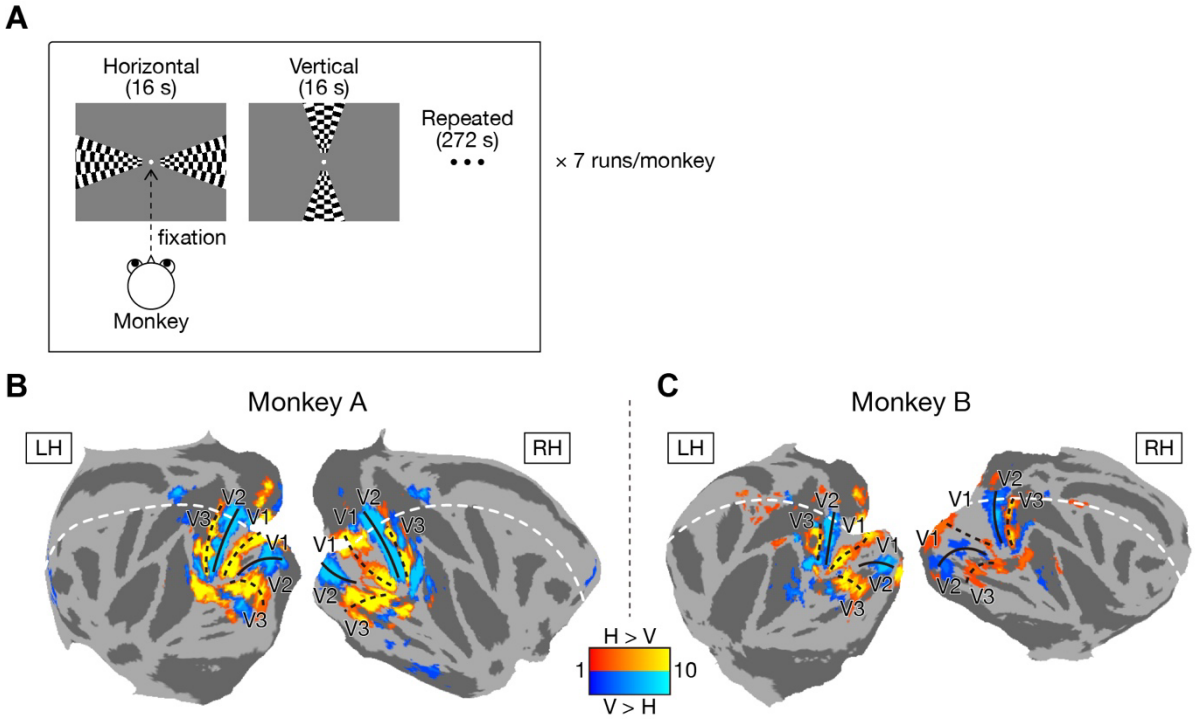

Figure 3.3. Activation maps to the meridian checker board stimuli.

(A) Schematic of the presented stimuli. The actual stimuli and experimental procedures are described in detail in the Methods section of Chapter 2 and in Figure 2.2C. (B) Cluster-corrected *t*-statistics maps of voxels that were significantly activated by either horizontal (warm colors) and the vertical (cold colors) wedges ($p < 0.005$, FWEc) overlayed on the cortical surfaces. The colorbar indicate *t*-values. The dashed and solid black lines indicate the estimated borders of visual areas. (C) Same as in B, but in monkey B.

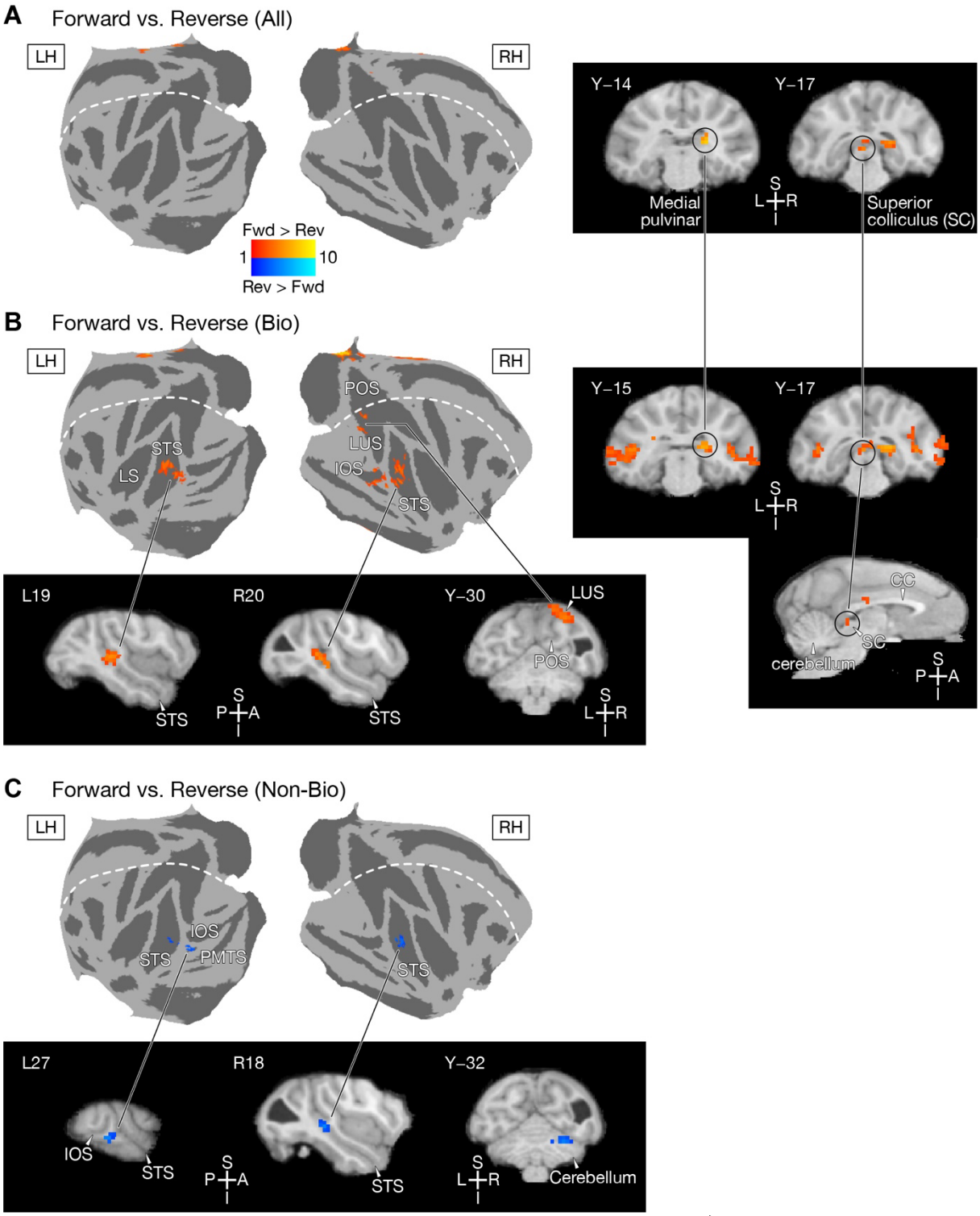

Figure 3.4. Whole brain activation of monkey A in Experiment 1 (Fwd≷Rev contrast).

(A) Left: A cluster-corrected *t*-statistics map of voxels with significant Forward > Reverse responses (warm colors, overlaid on the flattened cortical surface) across all videos (biological and non-biological). Right: Coronal slices showing significant clusters in subcortical regions: the right medial pulvinar and the left superior colliculus (SC). Numbers above each slice indicate coordinates in millimeters. No clusters survived the threshold for the Reverse > Forward contrast. The color bar indicates *t*-values. LH, left hemisphere; RH, right hemisphere. Table 1 lists all significant clusters. (B) Top left: Same as in A,

but for biological motion videos only. No clusters met the threshold for the Reverse > Forward contrast. Bottom left: Representative slices showing major clusters in the middle STS (both hemispheres) and the LUS (right hemisphere). Top right: Coronal slices showing significant clusters in the right medial pulvinar and the left SC, as observed in Panel A, but appearing larger. The left SC is also displayed on a sagittal slice. Table 2 lists all significant clusters. (C) Top: Same as in B, but for non-biological motion videos only. Cold colors indicate significant Reverse > Forward responses. No clusters survived for the Forward > Reverse contrast. Bottom: Representative slices showing clusters near the left STS, the right middle STS, and part of the cerebellum. Table 3 lists all significant clusters.

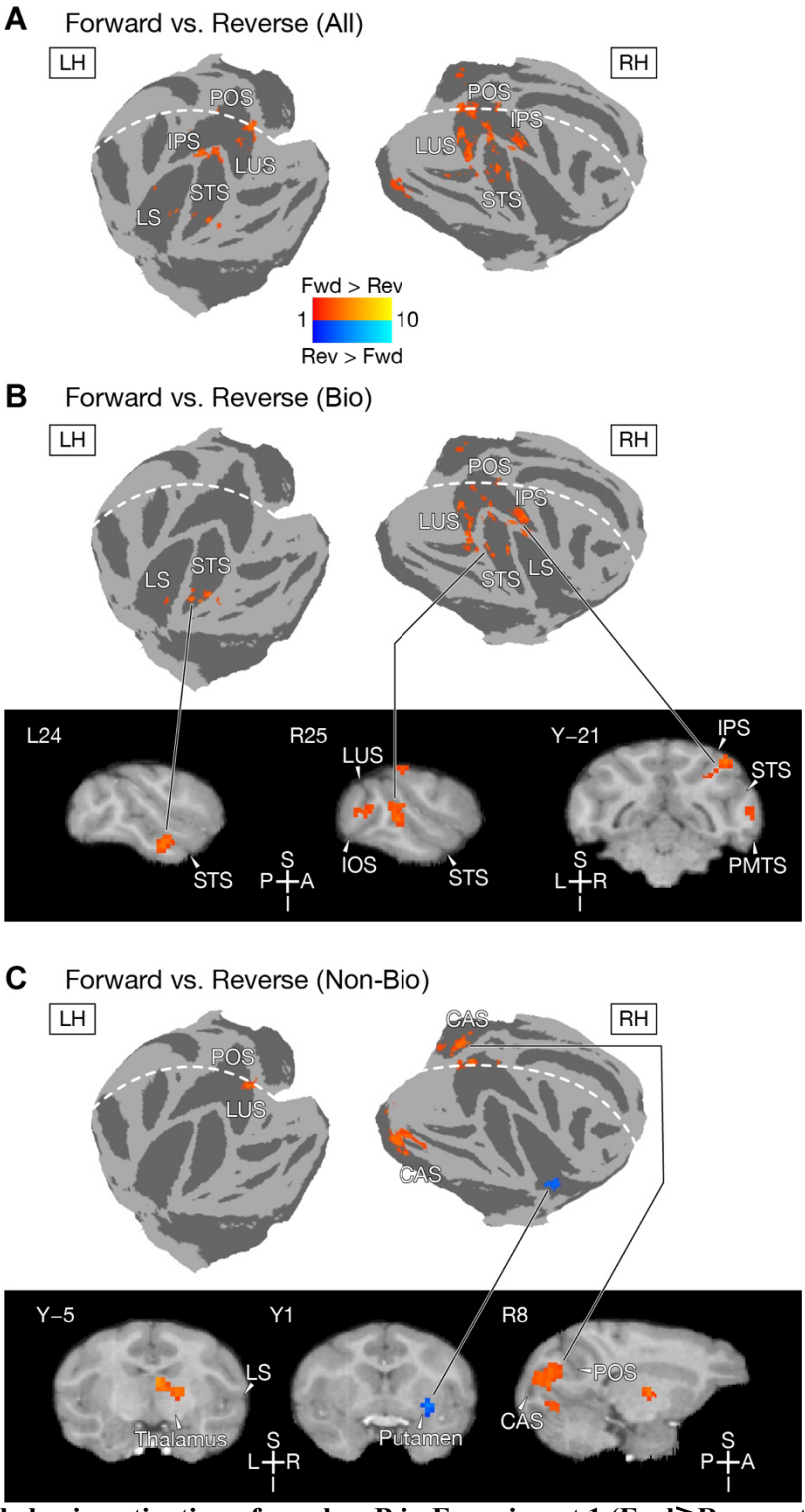

Figure 3.5. Whole brain activation of monkey B in Experiment 1 (Fwd≷Rev contrast).

(A) A cluster-corrected *t*-statistics map of voxels with significant Forward > Reverse responses across all videos, as in Figure 3A, but for monkey B. No clusters survived the threshold for the Reverse > Forward contrast. Table 4 lists all significant clusters. (B) Top: Same as in A, but for biological motion videos only. No clusters met the threshold for the Reverse > Forward contrast. Bottom: Representative slices showing major clusters in the left anterior STS, the right middle STS and the right IPS. Table 5 lists all significant clusters. (C) Top: Same as in B, but for non-biological motion videos only. Bottom:

Representative slices showing clusters in the right thalamus, the right putamen and the right CAS. Table 6 lists all significant clusters.

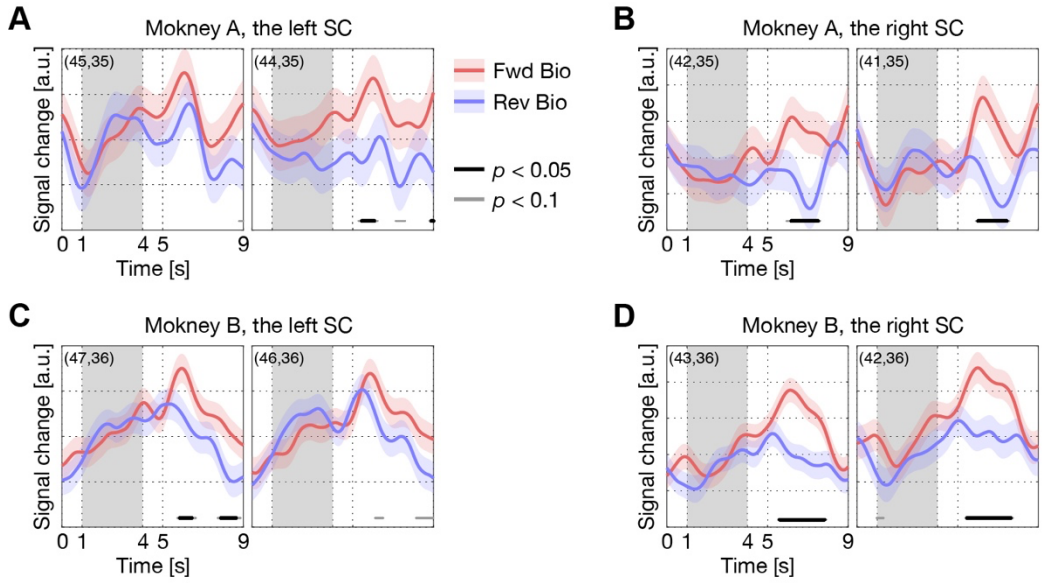

Figure 3.6. Averaged BOLD signals of individual voxels in the superior colliculus (SC) during forward and reverse biological video stimulus presentations.

(**A**) Averaged BOLD waveforms from two voxels in the left SC detected for monkey A in the Fwd>Rev contrast (All) and Fwd>Rev contrast (Bio). The red line represents the mean ± SE BOLD waveform for the forward biological condition, while the blue line represents the Reverse biological condition. The x-axis indicates time (seconds) from trial onset, and the y-axis represents signal change (a.u.). The gray-shaded area denotes the presentation period of video stimulus (3 s). A *t*-test was performed at each time point to compare the BOLD signals between the two conditions, with statistically significant differences indicated by black bars ($p < 0.05$) and gray bars ($p < 0.1$) below the graph. (**B**) Same as in **A**, but for the right SC of monkey A, from the same axial slice as in **A**. (**C**) Same as in **A**, but for the left SC of monkey B. (**C**) Same as in **A**, but for the right SC of monkey B.

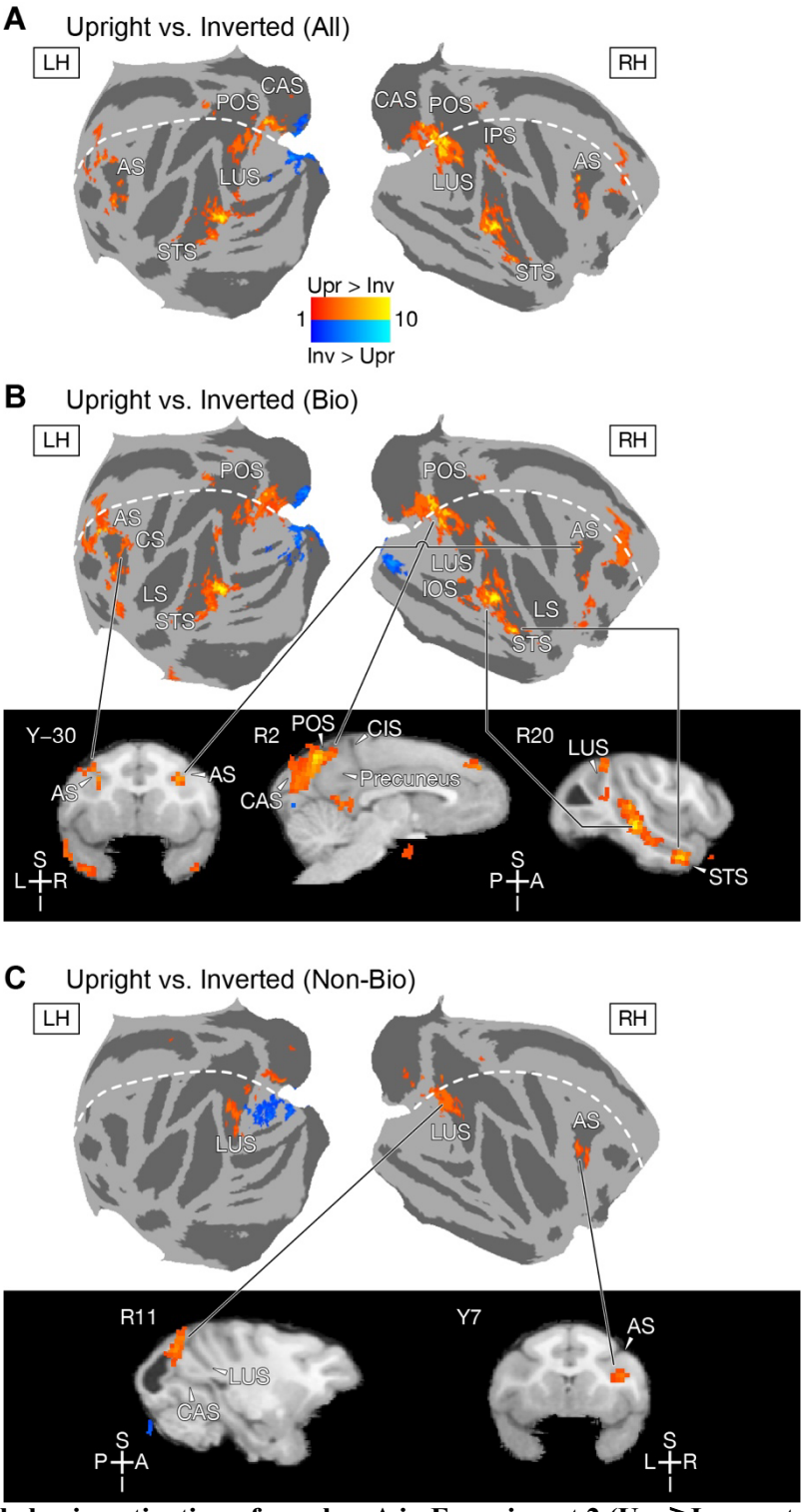

Figure 3.7. Whole brain activation of monkey A in Experiment 2 (Upr≷Inv contrast).

(A) A cluster-corrected *t*-statistics map of voxels with significant Upright > Inverted responses (warm colors) and Inverted > Upright (cold colors) responses across all videos (biological and non-biological), overlaid on the flattened cortical surface. The color bar indicates *t*-values. Table 7 lists all significant clusters. (B) Top: Same as in A, but for biological motion videos only. Bottom: Representative slices showing major clusters in the AS (both hemispheres), the right POS (Precuneus), and along the right STS. Table 8 lists all significant clusters. (C) Top: Same as in B, but for non-biological motion videos

only. Bottom: Representative slices showing clusters the left LUS and the right AS. Table 9 lists all significant clusters.

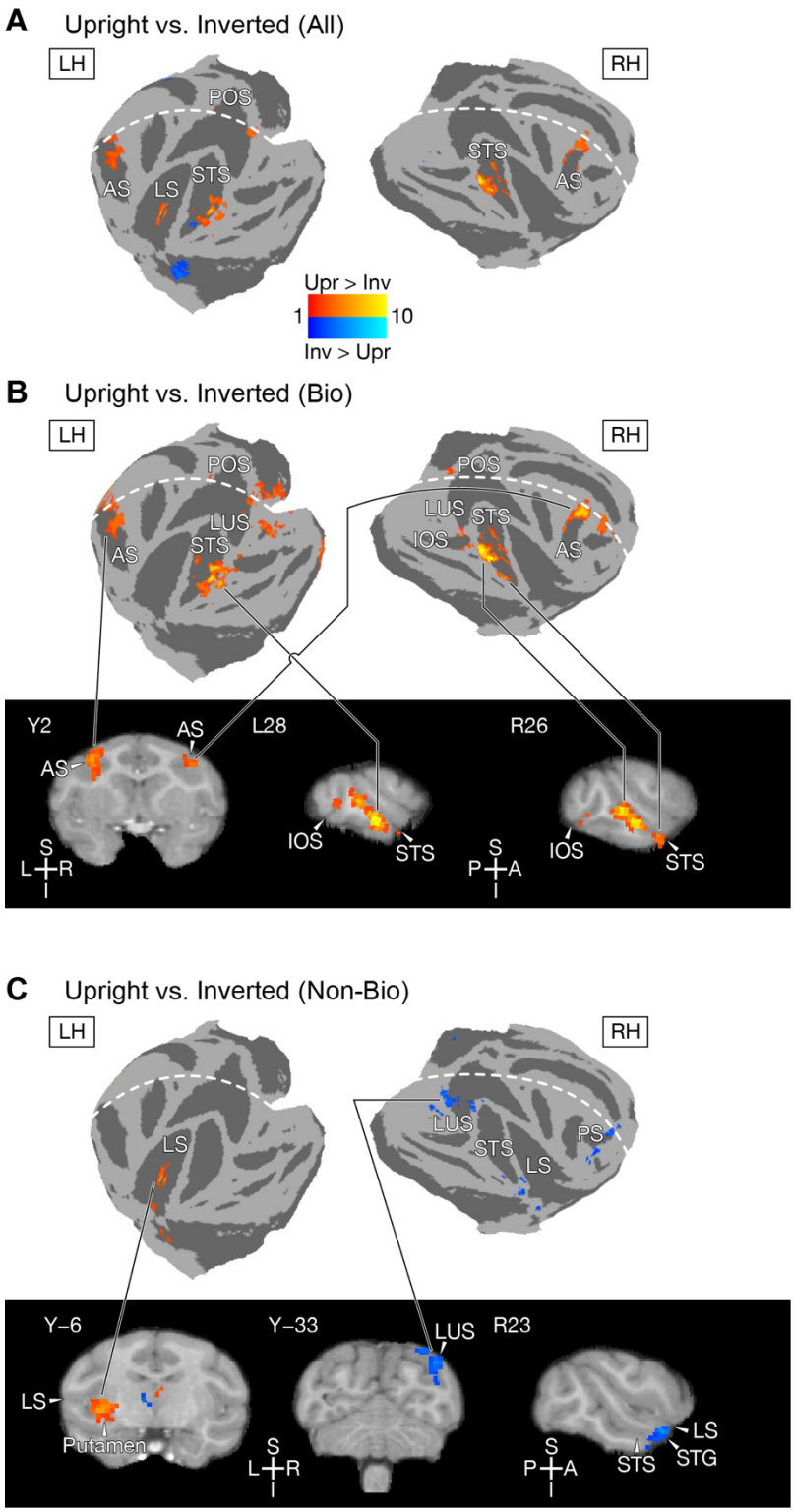

Figure 3.8. Whole brain activation of monkey B in Experiment 2 (Upr≷Inv contrast).

(A) A cluster-corrected *t*-statistics map of voxels with significant Upright > Inverted responses (warm colors) and Inverted > Upright (cold colors) responses across all videos (biological and non-biological), as in Figure 3.7A, but for monkey B. Table 10 lists all significant clusters. (B) Top: Same as in A, but for biological motion videos only. Bottom: Representative slices showing major clusters in the AS (both hemispheres) and along the STS (both hemispheres). Table 11 lists all significant clusters. (C) Top: Same

as in B, but for non-biological motion videos only. Bottom: Representative slices showing clusters in the left putamen (near the LS), the right LUS and the right rostral STG. Table 12 lists all significant clusters.

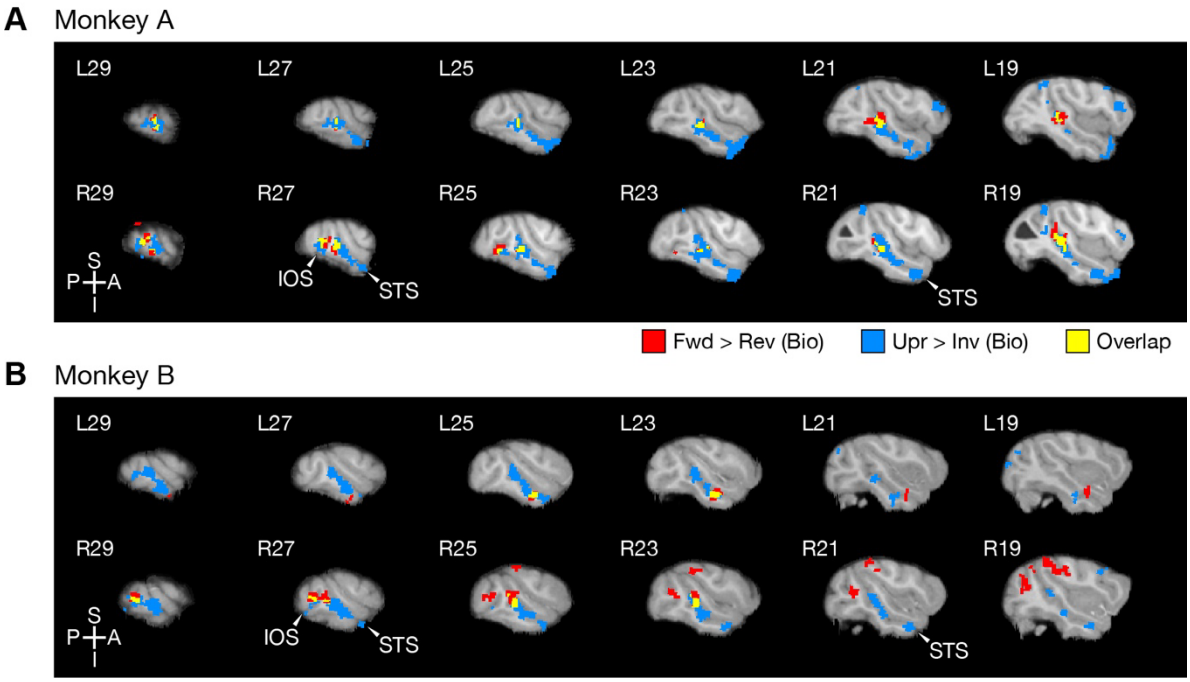

Figure 3.9. Comparison of clusters detected in the STS and IOS for the Forward > Reverse (Bio) and Upright > Inverted (Bio) contrasts.

(**A**) Activation maps for monkey A. Sagittal slices including the STS are shown for each hemisphere (Top: left hemisphere; Bottom: right hemisphere). Regions detected in the Fwd>Rev (Bio) contrast are shown in red, those detected in the Upr>Inv (Bio) contrast are shown in blue, and regions detected in both contrasts are shown in yellow. (**B**) Same as in **A**, but for monkay B.

Table 1. Clusters detected for Fwd≷Rev contrast (All) in monkey A

Region	Coordinate (mm)			peak-level			cluster-level		
	x	y	z	*t*-val	*p*	p_{FWE}	size	*p*	p_{FWE}
Forward > Reverse (All)									
(R) Medial pulvinar	9	-14	3	7.8	2.4×10^{-15}	1.1×10^{-10}	97	3.9×10^{-7}	4.1×10^{-5}
- (R) Thalamus(VL)	9	-8	2						
(L) Cerebellum	-15	-25	-10	5.2	1.2×10^{-7}	5.4×10^{-3}	6	0.099	1.00
Thalamus (VL)	-3	-9	4	5.0	2.5×10^{-7}	0.011	43	1.9×10^{-4}	0.020
(L) Superior colliculus	-2	-17	0	4.8	9.2×10^{-7}	0.042	2	0.33	1.00
Cerebellum (vermis)	2	-27	4	4.7	1.0×10^{-6}	0.047	29	1.4×10^{-3}	0.13
Reverse > Forward (All)									
No cluster									

Table 2. Clusters detected for Fwd≷Rev contrast (Bio) in monkey A

Region	Coordinate (mm)			peak-level			cluster-level		
	x	y	z	*t*-val	*p*	p_{FWE}	size	*p*	p_{FWE}
Forward > Reverse (Bio)									
(R) Medial pulvinar	9	-15	3	6.8	5.9×10^{-12}	2.7×10^{-7}	179	2.3×10^{-10}	2.4×10^{-8}
- (R) Thalamus(VL)	9	-8	2						
- (L) Superior colliculus	-2	-17	0						
(L) mSTS	-19	-16	2	5.3	6.5×10^{-8}	2.9×10^{-3}	66	1.1×10^{-5}	1.2×10^{-3}
(R) mSTS	20	-16	1	5.0	2.7×10^{-7}	0.012	128	1.9×10^{-8}	2.1×10^{-6}
(L) putamen	-11	-14	6	5.0	3.6×10^{-7}	0.016	5	0.13	1.00
(R) LUS (V2)	11	-30	17	4.7	1.0×10^{-6}	0.047	29	1.4×10^{-3}	0.13
Reverse > Forward (Bio)									
No cluster									

Table 3. Clusters detected for Fwd≷Rev contrast (Non-Bio) in monkey A

Region	Coordinate (mm)			peak-level			cluster-level		
	x	y	z	*t*-val	*p*	p_{FWE}	size	*p*	p_{FWE}
Forward > Reverse (Non-Bio)									
(R) Thalamus (VL)	10	-13	3	5.0	3.5×10^{-7}	0.016	41	2.4×10^{-4}	0.026
Reverse > Forward (Non-Bio)									
(R) mSTS	18	-15	0	5.0	3.2×10^{-7}	0.015	16	0.012	0.71
(L) mSTS/PMTS (TEO)	-27	-16	-4	4.9	4.7×10^{-7}	0.021	21	4.9×10^{-3}	0.40
(R) Cerebellum	11	-32	-5	4.8	9.7×10^{-7}	0.044	15	0.014	0.78

Table 4. Clusters detected for Fwd≷Rev contrast (All) in monkey B

Region	Coordinate (mm)			peak-level			cluster-level		
	x	y	z	t-val	p	p_{FWE}	size	p	p_{FWE}
Forward > Reverse (All)									
(L) aSTS	-25	-8	-9	5.0	2.4×10^{-7}	0.011	45	2.4×10^{-4}	0.023
(R) POS (V2)	2	-35	10	4.9	3.9×10^{-7}	0.017	251	4.1×10^{-12}	4.0×10^{-10}
- (R) LUS	11	-30	17						
- (L) pSTS	-13	-30	17						
- (L) IPS (LIP)	-18	-22	19						
(R) LUS	15	-35	10	4.5	3.5×10^{-6}	0.16	183	6.0×10^{-10}	5.8×10^{-8}
- (R) mSTS	25	-17	2						
(R) IPS (AIP/LIP)	17	-15	14	4.2	1.5×10^{-5}	0.69	59	4.6×10^{-5}	4.4×10^{-3}
Reverse > Forward (All)									
No cluster									

Table 5. Clusters detected for Fwd≷Rev contrast (Bio) in monkey B

Region	Coordinate (mm)			peak-level			cluster-level		
	x	y	z	t-val	p	p_{FWE}	size	p	p_{FWE}
Forward > Reverse (Bio)									
Out of brain	-27	-28	15	5.4	4.2×10^{-8}	1.9×10^{-3}	8	0.072	1.00
(L) aSTS	-24	-8	-9	4.9	4.2×10^{-7}	0.019	53	9.2×10^{-5}	8.8×10^{-3}
(R) LIP	19	-21	17	4.5	3.5×10^{-6}	0.16	88	2.2×10^{-6}	2.1×10^{-4}
(R) LUS	16	-35	10	4.4	4.5×10^{-6}	0.20	130	4.6×10^{-8}	4.4×10^{-6}
- (R) mSTS	25	-17	0						
(R) LIP/MST	11	-29	15	4.2	1.4×10^{-5}	0.61	41	4.0×10^{-4}	0.037
Reverse > Forward (Bio)									
No cluster									

Table 6. Clusters detected for Fwd≷Rev contrast (Non-Bio) in monkey B

Region	Coordinate (mm)			peak-level			cluster-level		
	x	y	z	t-val	p	p_{FWE}	size	p	p_{FWE}
Forward > Reverse (Non-Bio)									
(R) Thalamus	4	-5	4	5.7	5.8×10^{-9}	2.6×10^{-4}	37	6.7×10^{-4}	0.062
(R) CAS	8	-37	7	4.6	2.6×10^{-6}	0.12	152	7.1×10^{-9}	6.8×10^{-7}
Reverse > Forward (Non-Bio)									
(R) putammen	14	1	-3	5.0	3.5×10^{-7}	0.016	18	0.011	0.65

Table 7. Clusters detected for Upr≷Inv contrast (All) in monkey A

Region	Coordinate (mm)			peak-level			cluster-level		
	x	y	z	t-val	p	p_{FWE}	size	p	p_{FWE}
Upright > Inverted (All)									
V2	2	-32	19	9.4	0	0	554	7.6×10^{-21}	0
(R) mSTS	20	-13	-2	9.3	0	0	202	5.4×10^{-11}	5.6×10^{-9}
- (R) mSTS	20	-9	-9						
(L) mSTS	-27	-13	-2	9.0	0	0	237	3.8×10^{-12}	3.9×10^{-10}
- (L) aSTS	-26	-5	-9						
- (L) IOS	-24	-23	-1						
(L) Principal sulcus	-9	15	16	6.4	8.4×10^{-11}	3.8×10^{-6}	83	2.1×10^{-6}	2.2×10^{-4}
(R) aSTS	20	1	-13	6.1	6.6×10^{-10}	3.0×10^{-5}	56	4.3×10^{-5}	4.5×10^{-3}
(R) Arcuate sulcus	16	11	6	5.9	1.7×10^{-9}	7.9×10^{-5}	54	5.5×10^{-5}	5.7×10^{-3}
(L) Arcuate sulcus	-18	11	6	5.7	4.7×10^{-9}	2.2×10^{-4}	31	1.1×10^{-3}	0.11
(R) LIP	11	-21	18	5.4	3.4×10^{-8}	1.5×10^{-3}	33	8.5×10^{-4}	0.085
Out of brain	-1	-1	-11	5.0	3.0×10^{-7}	0.014	9	0.051	1.00
(L) Arcuate sulcus	-13	7	8	4.9	4.0×10^{-7}	0.018	5	0.13	1.00
Inverted > Upright (All)									
OP (/out of brain)	-4	-44	4	7.0	1.0×10^{-12}	4.7×10^{-8}	236	4.1×10^{-12}	4.2×10^{-10}
Out of brain	-11	-45	14	5.2	1.0×10^{-7}	4.6×10^{-3}	10	0.041	0.99

Table 8. Clusters detected for Upr≷Inv contrast (Bio) in monkey A

Region	Coordinate (mm)			peak-level			cluster-level		
	x	y	z	t-val	p	p_{FWE}	size	p	p_{FWE}
Upright > Inverted (Bio)									
(L) mSTS	-27	-13	-2	10.6	0	0	281	1.6×10^{-13}	1.7×10^{-11}
- (L) aSTS	-26	-5	-9						
(R) mSTS	22	-13	-2	10.0	0	0	381	2.1×10^{-16}	2.2×10^{-14}
- (R) aSTS	20	1	-13						
V2	2	-32	19	9.0	0	0	545	1.3×10^{-20}	0
Principal sulcus	-9	15	17	7.0	1.1×10^{-12}	5.1×10^{-8}	207	3.7×10^{-11}	3.8×10^{-9}
(L) Arcuate sulcus	-18	11	6	6.3	1.2×10^{-10}	5.6×10^{-6}	62	2.1×10^{-5}	2.2×10^{-3}
(R) Arcuate sulcus	13	6	12	6.1	6.3×10^{-10}	2.9×10^{-5}	8	0.064	1.00
(L) pSTS	-18	-23	17	5.7	6.5×10^{-9}	3.0×10^{-4}	29	1.5×10^{-3}	0.15
Out of brain	-1	0	-10	5.3	5.3×10^{-8}	2.4×10^{-3}	31	1.1×10^{-3}	0.11
(L) Arcuate sulcus	-14	5	13	5.2	8.2×10^{-8}	3.7×10^{-3}	25	2.8×10^{-3}	0.25
(R) pSTS	20	-22	16	5.0	3.5×10^{-7}	0.016	41	2.8×10^{-4}	0.029
(R) LIP	11	-21	18	4.9	4.0×10^{-7}	0.018	25	2.8×10^{-3}	0.25
Cerebellum/Thalamus	0	-23	4	4.8	7.4×10^{-7}	0.034	22	4.6×10^{-3}	0.38
(R) Arcuate sulcus	15	15	2	4.5	4.0×10^{-6}	0.18	49	1.0×10^{-4}	0.010
Inverted > Upright (Bio)									
Early visual cortex	-3	-39	4	7.0	1.4×10^{-12}	6.6×10^{-8}	148	4.5×10^{-9}	4.7×10^{-7}

Table 9. Clusters detected for Upr≷Inv contrast (Non-Bio) in monkey A

Region	Coordinate (mm)			peak-level			cluster-level		
	x	y	z	t-val	p	p_{FWE}	size	p	p_{FWE}
Upright > Inverted (Non-Bio)									
PCC	-7	-10	11	5.4	4.0×10^{-8}	1.8×10^{-3}	21	5.4×10^{-3}	0.43
(R) V2/V3	11	-33	15	5.3	5.1×10^{-8}	2.3×10^{-3}	177	4.0×10^{-10}	4.1×10^{-8}
(L) LUS (V2)	-17	-29	9	5.0	2.6×10^{-7}	0.012	81	2.6×10^{-6}	2.7×10^{-4}
(R) amygdala	5	-5	-14	4.9	3.9×10^{-7}	0.018	9	0.051	1.00
(R) Arcuate sulcus	17	8	7	4.5	2.8×10^{-6}	0.13	37	4.9×10^{-4}	0.049
(L) CAS	-4	-36	12	4.5	4.3×10^{-6}	0.19	43	2.2×10^{-4}	0.022
Inverted > Upright (Non-Bio)									
OP (/Out of brain)	-6	-45	0	5.5	1.4×10^{-8}	6.6×10^{-4}	514	7.3×10^{-20}	0

Table 10. Clusters detected for Upr≷Inv contrast (All) in monkey B

Region	Coordinate (mm)			peak-level			cluster-level		
	x	y	z	t-val	p	p_{FWE}	size	p	p_{FWE}
Upright > Inverted (All)									
(R) mSTS	27	-15	-1	9.0	0	0	144	1.3×10^{-9}	1.5×10^{-7}
- (R) mSTS	23	-12	-7						
(L) mSTS	-26	-11	-4	8.4	0	0	118	1.7×10^{-8}	1.9×10^{-6}
- (L) mSTS	-22	-17	-1						
- (L) aSTS	-25	-5	-10						
(L) Putammen	-17	-6	-1	6.0	9.9×10^{-10}	4.4×10^{-5}	68	4.1×10^{-6}	4.7×10^{-4}
(L) Arcuate sulcus	-14	2	15	5.5	1.9×10^{-8}	8.5×10^{-4}	41	1.4×10^{-4}	0.016
(R) Arcuate sulcus	11	7	18	5.3	5.9×10^{-8}	2.6×10^{-3}	64	6.7×10^{-6}	7.6×10^{-4}
(L) Thalamus (MD)	-2	-8	2	5.3	6.8×10^{-8}	3.0×10^{-3}	5	0.11	1.00
Out of brain	10	-41	18	5.0	3.4×10^{-7}	0.015	2	0.31	1.00
(L) POS (V2)	-3	-35	16	4.8	8.5×10^{-7}	0.038	19	5.0×10^{-3}	0.43
Inverted > Upright (All)									
(L) PCC	-7	-10	11	5.5	2.3×10^{-8}	1.0×10^{-3}	8	0.051	1.00
Out of brain (V1)	18	-44	-6	4.9	5.7×10^{-7}	0.026	14	0.013	0.78
(L) Putamen	-10	-5	-8	4.7	1.5×10^{-6}	0.066	35	3.5×10^{-4}	0.039

Table 11. Clusters detected for Upr≷Inv contrast (Bio) contrast in monkey B

Region	Coordinate (mm)			peak-level			cluster-level		
	x	y	z	t-val	p	p_{FWE}	size	p	p_{FWE}
Upright > Inverted (Bio)									
(L) mSTS	-28	-11	-5	12.2	0	0	212	3.2×10^{-12}	3.6×10^{-10}
- (L) mSTS	-28	-17	1						
- (L) IOS	-28	-24	1						
(R) mSTS	26	-15	-2	11.5	0	0	218	1.9×10^{-12}	2.2×10^{-10}
- (R) mSTS	23	-13	-7						
- (R) LUS	29	-23	0						
(R) Arcuate sulcus	9	8	19	7.6	1.1×10^{-14}	4.7×10^{-10}	93	2.3×10^{-7}	2.6×10^{-5}
(R) aSTS	21	-1	-12	6.9	2.4×10^{-12}	1.1×10^{-7}	42	1.2×10^{-4}	0.014
(L) AS	-15	2	14	6.2	2.5×10^{-10}	1.1×10^{-5}	50	4.1×10^{-5}	4.6×10^{-3}
(R) 9d	5	19	16	6.2	3.5×10^{-10}	1.6×10^{-5}	62	8.6×10^{-6}	9.8×10^{-4}
(L) OFC	-3	24	4	5.0	2.6×10^{-7}	0.012	32	5.5×10^{-4}	0.061
(L) AS (8B)	-8	12	17	4.7	1.0×10^{-6}	0.047	33	4.7×10^{-4}	0.052
(L) CAS	-17	-40	6	3.8	6.2×10^{-5}	1.0	142	1.6×10^{-9}	1.8×10^{-7}
Inverted > Upright (Bio)									
No cluster									

Table 12. Clusters detected for Upr≷Inv contrast (Non-Bio)) in monkey B

Region	Coordinate (mm)			peak-level			cluster-level		
	x	y	z	t-val	p	p_{FWE}	size	p	p_{FWE}
Upright > Inverted (Non-Bio)									
Thalamus (MD)	-1	-7	3	6.2	2.8×10^{-10}	1.2×10^{-5}	7	0.066	1.00
(L) Putamen	-16	-6	-1	6.2	3.0×10^{-10}	1.4×10^{-5}	91	2.9×10^{-7}	3.3×10^{-5}
- (L) Globus pallidus	-11	-3	-2						
(L) F3	-3	6	19	5.2	1.1×10^{-7}	4.7×10^{-3}	3	0.21	1.00
Inverted > Upright (Non-Bio)									
(R) rSTG	23	3	-9	5.6	1.3×10^{-8}	5.9×10^{-4}	36	3.0×10^{-4}	0.033
Thalamus	-2	-4	1	5.0	3.7×10^{-7}	0.017	5	0.11	1.00
Out of brain (V1)	18	-44	-6	4.9	4.1×10^{-7}	0.019	11	0.025	0.94
(R) LUS	18	-33	13	4.9	4.3×10^{-7}	0.019	69	3.6×10^{-6}	4.1×10^{-4}
PCC/caudate	-6	-9	10	4.7	1.1×10^{-6}	0.050	17	7.3×10^{-3}	0.56
(R) PS	5	23	9	4.2	1.3×10^{-5}	0.57	78	1.2×10^{-6}	1.4×10^{-4}
(R) amygdala	10	3	-12	3.9	5.4×10^{-5}	1.0	39	1.9×10^{-4}	0.021

3.6. References

Adachi, I., Chou, D. P., & Hampton, R. R. (2009). Thatcher Effect in Monkeys Demonstrates Conservation of Face Perception across Primates. *Current Biology*, 19(15), 1270–1273.

Andersson, J. L. R., Skare, S., & Ashburner, J. (2003). How to correct susceptibility distortions in spin-echo echo-planar images: Application to diffusion tensor imaging. *NeuroImage*, 20(2), 870–888.

Ashburner, J. (2012). SPM: A history. *NeuroImage*, 62(2), 791–800.

Balan, P. F., Gerits, A., Zhu, Q., Kolster, H., Orban, G. A., Wardak, C., & Vanduffel, W. (2019). Fast Compensatory Functional Network Changes Caused by Reversible Inactivation of Monkey Parietal Cortex. *Cerebral Cortex*, 29(6), 2588–2606.

Berman, R. A., & Wurtz, R. H. (2010). Functional identification of a pulvinar path from superior colliculus to cortical area MT. *Journal of Neuroscience*, 30(18), 6342–6354.

Bogadhi, A. R., Katz, L. N., Bollimunta, A., Leopold, D. A., & Krauzlis, R. J. (2021). Midbrain activity shapes high-level visual properties in the primate temporal cortex. *Neuron*, 109(4), 690-699.e5.

Ding, X., Yin, J., Shui, R., Zhou, J., & Shen, M. (2017). Backward-walking biological motion orients attention to moving away instead of moving toward. *Psychonomic Bulletin & Review*, *24*(2), 447–452.

Duncan, J., Humphreyst, G., & Ward, R. (1997). Competitive brain activity in visual attention Abbreviation SLAM selective attention model. *Current Opinion in Neurobiology*, 7(2), 255–261.

Friston, K. (2012). The history of the future of the Bayesian brain. *NeuroImage*, 62(2), 1230–1233.

Fujisaki, W., Shimojo, S., Kashino, M., & Nishida, S. (2004). Recalibration of audiovisual simultaneity. *Nature Neuroscience*, 7(7), 773–778.

Goldstein, R., Bauer, L. O., & Stern, J. A. (1992). Effect of task difficulty and interstimulus interval on blink parameters. *International Journal of Psychophysiology*, 13(2), 111–117.

Grèzes, J., Fonlupt, P., Bertenthal, B., Delon-Martin, C., Segebarth, C., & Decety, J. (2001). Does perception of biological motion rely on specific brain regions? *NeuroImage*, 13(5), 775–785.

Grossman, E. D., & Blake, R. (2001). Brain activity evoked by inverted and imagined biological motion. *Vision Research*, 41(10–11), 1475–1482.

Hanyu, N., Watanabe, K., & Kitazawa, S. (2023a). Ready to detect a reversal of time's arrow: a psychophysical study using short video clips in daily scenes. *Royal Society Open Science*, 10(4).

Hanyu, N., Watanabe, K., & Kitazawa, S. (2023b, October 4). Neural bases for judging the direction of time's arrow. *Proceedings Timing Research Forum 3*, Champalimaud Center for the Unknown, Lisbon, Portugal.

Heed, T., & Azañón, E. (2014). Using time to investigate space: A review of tactile temporal order judgments as a window onto spatial processing in touch. *Frontiers in Psychology*, 5(76).

Hikosaka, O., Miyauchi, S., & Shimojot, S. (1993). Focal Visual Attention Produces Illusory Temporal Order and Motion Sensation. *Vision Research*, 33(9), 1219–1240.

Hirsh, I. J., & Sherrick, C. E. , Jr. (1961). Perceived order in different sense modalities. *Journal of Experimental Psychology*, 62(5), 423–432.

Knill, D. C., & Pouget, A. (2004). The Bayesian brain: The role of uncertainty in neural coding and computation. *Trends in Neurosciences*, 27(12), 712–719.

Leite, F. P., Tsao, D., Vanduffel, W., Fize, D., Sasaki, Y., Wald, L. L., Dale, A. M., Kwong, K. K., Orban, G. A., Rosen, B. R., Tootell, R. B. H., & Mandeville, J. B. (2002). Repeated fMRI using iron oxide contrast agent in awake, behaving macaques at 3 Tesla. *NeuroImage*, 16(2), 283–294.

Lu, X., Hu, Z., Xin, Y., Yang, T., Wang, Y., Zhang, P., Liu, N., & Jiang, Y. (2024). Detecting biological motion signals in human and monkey superior colliculus: a subcortical-cortical pathway for biological motion perception. *Nature Communications*, 15(1), 9606.

Maffei, V., Giusti, M. A., Macaluso, E., Lacquaniti, F., & Viviani, P. (2015). Unfamiliar Walking Movements Are Detected Early in the Visual Stream: An fMRI Study. Cerebral Cortex, 25(8), 2022–2034.

Miyazaki, M., Yamamoto, S., Uchida, S., & Kitazawa, S. (2006). Bayesian calibration of simultaneity in tactile temporal order judgment. *Nature Neuroscience*, 9(7), 875–877.

Monfort, M., Andonian, A., Zhou, B., Ramakrishnan, K., Bargal, S. A., Yan, T., Brown, L., Fan, Q.,

Gutfreund, D., Vondrick, C., & Oliva, A. (2020). Moments in Time Dataset: One Million Videos for Event Understanding. *IEEE Transactions on Pattern Analysis and Machine Intelligence*, 42(2), 502–508.

Nishimoto, S., Vu, A. T., Naselaris, T., Benjamini, Y., Yu, B., & Gallant, J. L. (2011). Reconstructing visual experiences from brain activity evoked by natural movies. *Current Biology*, 21(19), 1641–1646.

Oram, M. W., & Perrett, D. I. (1994). Responses of anterior superior temporal polysensory (STPa) neurons to "biological motion" stimuli. *Journal of Cognitive Neuroscience*, 6(2), 99–116.

Oram, M. W., & Perrett, D. I. (1996). Integration of Form and Motion in the Anterior Superior Temporal Polysensory Area (STPa) of the Macaque Monkey. *Journal of Neurophysiology*, 76(1), 109–129.

Pinsk, M. A., Arcaro, M., Weiner, K. S., Kalkus, J. F., Inati, S. J., Gross, C. G., & Kastner, S. (2009). Neural representations of faces and body parts in macaque and human cortex: A comparative fMRI study. *Journal of Neurophysiology*, 101(5), 2581–2600.

Pöppel, E. (1997). A hierarchical model of temporal perception. *Trends in Cognitive Sciences*, 1(2), 56–61.

Premereur, E., Vanduffel, W., & Janssen, P. (2014). The Effect of FEF Microstimulation on the Responses of Neurons in the Lateral Intraparietal Area. *Journal of Cognitive Neuroscience*, 26(8), 1672–1684.

Shi, J., Weng, X., He, S., & Jiang, Y. (2010). Biological motion cues trigger reflexive attentional orienting. *Cognition*, *117*(3), 348–354.

Shore, D. I., Spence, C., & Klein, R. M. (2001). Visual Prior Entry. *Psychological Science*, 12(3), 205–212.

Shore, D. I., Spry, E., & Spence, C. (2002). Confusing the mind by crossing the hands. *Cognitive Brain Research*, 14(1), 153–163.

Smith, S. M., Jenkinson, M., Woolrich, M. W., Beckmann, C. F., Behrens, T. E. J., Johansen-Berg, H., Bannister, P. R., De Luca, M., Drobnjak, I., Flitney, D. E., Niazy, R. K., Saunders, J., Vickers, J., Zhang, Y., De Stefano, N., Brady, J. M., & Matthews, P. M. (2004). Advances in functional and structural MR image analysis and implementation as FSL. *NeuroImage*, 23, S208–S219.

Suda, Y., & Kitazawa, S. (2015). A model of face selection in viewing video stories. *Scientific Reports*, *5*(1), 7666.

Sugita, Y., & Suzuki, Y. (2003). Implicit estimation of sound-arrival time. *Nature*, 421(911), 911–912.

Tada, H., Omori, Y., Hirokawa, K., Ohira, H., & Tomonaga, M. (2013). Eye-Blink Behaviors in 71 Species of Primates. *PLoS ONE*, 8(5), e66018.

Tanaka, R., Watanabe, K., Suzuki, T., Nakamura, K., Yasuda, M., Ban, H., Okada, K., & Kitazawa, S. (2024). An easy-to-implement , non-invasive head restraint method for monkey fMRI. *NeuroImage*, 285, 120479.

Thompson, P. G. (1980). Margaret Thatcher: A new illusion. *Perception*, 9(4), 483–484.

Van Essen, D. C., Drury, H. A., Dickson, J., Harwell, J., Hanlon, D., & Anderson, C. H. (2001). An integrated software suite for surface-based analyses of cerebral cortex. *Journal of the American Medical Informatics Association*, 8(5), 443–459.

Vanduffel, W., Fize, D., Mandeville, J. B., Nelissen, K., Van Hecke, P., Rosen, B. R., Tootell, R. B. H., & Orban, G. A. (2001). Visual motion processing investigated using contrast agent-enhanced fMRI in awake behaving monkeys. *Neuron*, 32(4), 565–577.

Wang, Y., Zhang, X., Wang, C., Huang, W., Xu, Q., Liu, D., Zhou, W., Chen, S., & Jiang, Y. (2022). Modulation of biological motion perception in humans by gravity. *Nature Communications*, 13(1), 1–10.

Wardak, C., Olivier, E., & Duhamel, J. R. (2011). The relationship between spatial attention and saccades in the frontoparietal network of the monkey. *European Journal of Neuroscience*, 33(11), 1973–1981.

Yamamoto, S., & Kitazawa, S. (2001). Reversal of subjective temporal order due to arm crossing. *Nature Neuroscience*, 4(7), 759–765.

Chapter 4
General Discussion

In this dissertation, I investegated the neural bases underlying the discrimination of time's arrow by awake monkeys fMRI, alongside the development of a non-invasive head restraint system. Together, these contributions addressed fundamental challenges in studying the primate brain and provide notable perspectives on temporal cognition. The methodological advancements presented in Chapter 2 enabled stable, high-quality data acquisition in awake monkeys fMRI without invasive procedures, overcoming previous technical and ethical limitations. Building on this foundation, the experimental findings in Chapter 3 identified neural circuits in the superior temporal sulcus (STS), superior colliculus (SC), medial pulvinar, and cerebellum contributing to processing temporal dynamics in visual motion stimuli. By integrating these methodological and experimental advances, this dissertation provides a robust framework for investigating the neural basis of time perception in primates.

Advancements in Methodology of Awake Monkey fMRI

The non-invasive head restraint system developed in Chapter 2 enabled stable and reliable fMRI data acquisition in awake monkeys. This thermoplastic mask minimized motion artifacts and enhanced animal welfare by avoiding surgical procedures. By thoroughly validating its ability to measure reliable activation in the visual cortex, it addressed longstanding challenges in awake monkey imaging. Additionally, the mask aligns with ethical principles by reducing distress and avoiding invasive techniques, and its cost-effectiveness makes it accessible to a wide range of researchers. Moreover, the system's adaptability supports longer scanning sessions and integration with other neuroscience techniques (e.g., elecrtophysiological neural recording), paving the way for more comprehensive studies in the future.

Neural Bases for Discriminating Time's Arrow

The primary experimental findings in Chapter 3 emphasized the role of specific brain regions in processing the directionality of time's arrow. The superior temporal sulcus (STS), superior colliculus (SC), and medial pulvinar were identified as key areas involved in detecting forward biological motion. These findings indicate that the STS is highly sensitive to temporally coherent biological dynamics, with subcortical inputs from the SC and medial pulvinar enhancing its processing capabilities. Furthermore, reverse playback of non-biological motion activated a distinct network, including the cerebellum and portions of the STS, which appear to detect violations of physical plausibility through prediction-error mechanisms. These results emphasize the primate brain's ability to categorize and evaluate temporal information based on biological and physical plausibility. Additionally, within the STS, while there was some overlap between the regions preferring forward biological motion and those preferring upright

biological motion, certain areas exhibited selectivity exclusively for one or the other (Figure 3.9). This suggests that while the STS as a whole detects the spatiotemporal plausibility of biological motion, the posterior portion of the middle STS exhibits specific selectivity for the temporal direction of biological motion, supporting the notion that this region embodies the concept of “time’s arrow.”

Differences Between Monkey and Human fMRI Findings

In this study, we identified the STS, SC, and pulvinar as regions exhibiting a preference for forward motion, while the STS and cerebellum were detected as regions preferentially responding to reverse motion. Notably, the forward-preferential responses in the STS and SC were robust and consistently observed across both monkeys tested. In contrast, the reverse-preferential response was detected in only one monkey. On the other hand, previous human fMRI studies did not identify few brain regions exhibiting a preference for forward motion. Instead, biological motion areas such as the STS and middle temporal gyrus (MTG), as well as the cerebellum, showed preferential responses to reverse playback (Hanyu et al., 2023b, conference presentation; Maffei et al., 2015). These findings suggest that the neural mechanisms underlying the discrimination of time’s arrow differ between species, with a forward-preferential response observed in the monkey brain and a reverse-preferential response observed in the human brain.

This discrepancy is likely attributable to differences in experimental design. In our monkey study, visual stimuli were presented passively, whereas in human studies, participants were required to judge the playback direction (forward or reverse) after stimulus presentation. Behavioral experiments in humans have demonstrated that when participants are given such a discrimination task, they tend to perceive a video as forward unless there is a decisive cue indicating reversal. When such cues are present, they can immediately recognize the video as reversed. Consequently, in human fMRI studies where a playback direction discrimination task was employed, participants likely directed strong attention toward detecting features indicative of reversed playback, leading to an enhanced brain activity to reverse motion.

Therefore, if monkeys were required to perform a forward/reverse discrimination task, it is possible that, similar to humans, their responses to reverse playback would be enhanced, making the reverse-preferential response detected in the STS and cerebellar more robust. Conversely, if humans were to passively view the stimuli without performing a task, their response to reverse playback might diminish, while their response to forward playback could become more pronounced. However, training monkeys to discriminate playback direction is challenging, and excessive training may lead them to develop an artificial, task-specific viewing strategy that differs fundamentally from the strong perceptual dissonance humans experience when viewing reversed videos. Thus, careful consideration is required when designing experiments to assess temporal direction discrimination in non-human primates.

Acquisition of the Concept of "Time's Arrow"

Behavioral experiments in our laboratory identified specific cues for discriminating playback direction, including forward motion, falling, diffusion, division, and addition. These cues likely stem from

acquired beliefs about how objects and organisms naturally move, shaped by everyday experiences such as the constant downward force of gravity and interactions with directional entities like animals and vehicles. For example, a professional musician might detect reversed playback from unnatural breathing patterns or inferred melodies, whereas an untrained observer may not.

The monkeys in this study were laboratory-housed, meaning their experiences differ from those of wild monkeys. To ensure that monkeys could reasonably interpret the video stimuli, we used videos featuring biological motion and natural physical changes (e.g., falling fruit, water diffusion). In particular, for biological motion, the monkeys demonstrated a tendency to gaze intently at the faces and bodies of animals, directing strong attention to biological motion, which may have contributed to the robust forward-preferential responses.

An interesting prior study using chicks provides additional insights. In this study, chicks reared in complete darkness after hatching preferred intact point-light displays of walking chickens over scrambled versions. Additionally, a study on human neonates reported that newborns exhibited a preference for point-light displays of biological motion but did not show interest when the stimuli were presented upside down. These results imply that the concept of "time's arrow" may not be solely learned but could be an intrinsic function of the brain. Evolutionarily conserved structures like the SC and pulvinar, which exhibited forward-preferential responses in this study, may play a key role. Future research with human neonates and environmentally controlled monkeys could clarify the extent to which temporal directionality is innate.

Implications and Future Directions

The findings of this dissertation have several important implications. First, the development of a non-invasive head restraint system presents opportunities for broader applications, including its adaptation to other species and additional methods for recording brain and neural responses, which could significantly advance animal neuroscience research. Second, the involvement of the SC–pulvinar–STS pathway in temporal processing highlights the importance of subcortical–cortical interactions, suggesting that time’s arrow perception is a primal sense that relies on information processing in evolutionarily ancient brain regions (i.e., the SC and pulvinar). Third, the cerebello-cortical network, functioning as a prediction-error detector, also appears to be involved in detecting unexpected reversed motion. Electrophysiological recordings of neural responses in these networks are needed to investigate the mechanisms of time’s arrow perception in greater detail. Because our group has reported that humans can judge the direction of time’s arrow in as little as 300 ms, fMRI measurements alone are insufficient to fully elucidate its underlying neural substrate. Finally, the shared mechanisms for time’s arrow discrimination in humans and monkeys – evidenced by involvement of the cerebello-cortical network – suggest that temporal cognition is evolutionarily conserved among primates. After completing the ongoing human fMRI study in our laboratory, it will be valuable to compare brain activations across species to elucidate information-processing mechanisms conserved through evolution, as well as the higher-order functions uniquely acquired by humans. In this study, I obtained several important insights

into the recognition function of temporal “directionality,” a fundamental characteristic of time, and established plans for further elucidating the neural basis of temporal cognition in primates.

References

Hanyu, N., Watanabe, K., & Kitazawa, S. (2023a). Ready to detect a reversal of time’s arrow: a psychophysical study using short video clips in daily scenes. *Royal Society Open Science*, 10(4).

Hanyu, N., Watanabe, K., & Kitazawa, S. (2023b, October 4). Neural bases for judging the direction of time’s arrow. *Proceedings Timing Research Forum 3*, Champalimaud Center for the Unknown, Lisbon, Portugal.

Maffei, V., Giusti, M. A., Macaluso, E., Lacquaniti, F., & Viviani, P. (2015). Unfamiliar Walking Movements Are Detected Early in the Visual Stream: An fMRI Study. Cerebral Cortex, 25(8), 2022–2034.

Chapter 5
Achievements

5.1. Papers

Tanaka, R., Watanabe, K., Suzuki, T., Nakamura, K., Yasuda, M., Ban, H., Okada, K., and Kitazawa, S. (2024). An easy-to-implement, non-invasive head restraint method for monkey fMRI. *Neuroimage*, 285:120479.

Tanaka, R., Watanabe, K., Ban, H., and Kitazawa, S. Neural Bases for Discriminating the Temporal Direction of Time's Arrow: An Awake Monkey fMRI Study. (under review)

5.2. Presentations

Tanaka, R., Watanabe, K., Ban, H., Okada, K., and Kitazawa, S. A non-invasive method to prevent head movements of awake monkeys during event-related fMRI. *The 27th Annual Meeting of OHBM 2021*. Online. 2021/6/21-25.

Watanabe, K., Tanaka, R., Ban, H., Okada, K. and Kitazawa S. A non-invasive method to prevent head movements of awake monkeys during event-related fMRI. *The 44th Annual Meeting of the Japan Neuroscience Society*. Kobe. 2021/7/28-31.

Reiji Tanaka, Nao Hanyu, Kei Watanabe, Shigeru Kitazawa. *International Symposium on 'Chronogenesis'*. Okinawa. 2022/2/12–13.

田中 澪士, 渡邉 慶, 鈴木 隆文, 番 浩志, 北澤 茂. 覚醒行動中のサルにおける完全に非侵襲な fMRI 計測法. *第 115 回近畿生理学会談話会*. 大阪. 2023/11/11.

Reiji Tanaka, Hiroshi Ban, Kei Watanabe, Shigeru Kitazawa. Primate temporal cortices preferentially encode biological motion that are more physically plausible: an fMRI stud. *NEURO2024*. Fukuoka. 2024/7/24–27.